

EARLIEST STAGES OF PROTOCLUSTER FORMATION: SUBSTRUCTURE AND KINEMATICS OF STARLESS CORES IN ORION

KATHERINE LEE¹, LESLIE W. LOONEY^{1,2}, SCOTT SCHNEE², AND ZHI-YUN LI³

¹ Department of Astronomy, University of Illinois, Urbana, IL 61801, USA

² National Radio Astronomy Observatory, Charlottesville, VA 22903, USA

³ Astronomy Department, University of Virginia, Charlottesville, VA 22904, USA

Received 2013 March 5; accepted 2013 June 7; published 2013 July 11

ABSTRACT

We study the structure and kinematics of nine 0.1 pc scale cores in Orion with the IRAM 30 m telescope and at higher resolution eight of the cores with CARMA, using CS(2–1) as the main tracer. The single-dish moment zero maps of the starless cores show single structures with central column densities ranging from 7 to $42 \times 10^{23} \text{ cm}^{-2}$ and LTE masses from $20 M_{\odot}$ to $154 M_{\odot}$. However, at the higher CARMA resolution ($5''$), all of the cores except one fragment into 3–5 components. The number of fragments is small compared to that found in some turbulent fragmentation models, although inclusion of magnetic fields may reduce the predicted fragment number and improve the model agreement. This result demonstrates that fragmentation from parsec-scale molecular clouds to sub-parsec cores continues to take place inside the starless cores. The starless cores and their fragments are embedded in larger filamentary structures, which likely played a role in the core formation and fragmentation. Most cores show clear velocity gradients, with magnitudes ranging from 1.7 to $14.3 \text{ km s}^{-1} \text{ pc}^{-1}$. We modeled one of them in detail, and found that its spectra are best explained by a converging flow along a filament toward the core center; the gradients in other cores may be modeled similarly. We infer a mass inflow rate of $\sim 2 \times 10^{-3} M_{\odot} \text{ yr}^{-1}$, which is in principle high enough to overcome radiation pressure and allow for massive star formation. However, the core contains multiple fragments, and it is unclear whether the rapid inflow would feed the growth of primarily a single massive star or a cluster of lower mass objects. We conclude that fast, supersonic converging flow along filaments play an important role in massive star and cluster formation.

Key words: ISM: clouds – radio lines: stars – stars: formation – stars: massive

Online-only material: color figures

1. INTRODUCTION

Star formation involves a complicated interplay between turbulence, magnetic fields, and gravity. While the understanding of low-mass star formation has advanced over decades (e.g., McKee & Ostriker 2007), that of massive star formation has progressed more slowly. One difficulty is that massive protostars generate a much stronger radiation pressure that can strongly modify the gas accretion in the formation process (see Zinnecker & Yorke 2007). Another is that massive stars appear to form in crowded environments of clusters (Lada & Lada 2003). This study aims to understand the conditions for massive star formation and their clustered environment at early stages.

There are two main competing scenarios in massive star formation. One of them is the “turbulent core model” proposed by McKee & Tan (2003). In this model, the core is supported by supersonic turbulence and evolves on several free-fall timescale. The turbulent core is in quasi-static equilibrium and the formation of massive stars is a scaled-up version of low-mass star formation. The final mass of a massive star is determined by the mass of its natal core and the stellar environment is unimportant. The high pressure caused by supersonic turbulence results in high accretion rate ($>10^{-3} M_{\odot} \text{ yr}^{-1}$), overcoming the radiation pressure and continuing accretion process. In this model, the collapse is envisioned to be more or less monolithic with a relatively low level of fragmentation.

Alternatively, Bonnell et al. (2004) and Bonnell & Bate (2006) proposed that massive star formation is a dynamical process that involves competitive accretion. In a core that is dominated by supersonic turbulent motions, significant density

fluctuations are generated due to turbulent support with gravity taking over in the densest regions. Stellar seeds are created through this “turbulent fragmentation” and eventually lead to clusters. Massive stars form from the seeds located near the center of the cluster where the gravitational potential is deepest; these seeds win the competition for the reservoir of gas to grow to the highest masses. In this scenario, the final mass of a massive star is strongly influenced by their environment and has little correlation with the initial mass of the natal core.

A major difference of the two scenarios, which can be tested observationally, is the level of fragmentation. The turbulent core scenario envisions the existence of one massive starless core, while the competitive accretion scenario requires a higher level of fragmentation in massive starless cores. Therefore, our goal is to study the fragmentation in starless cores, the earliest stage of star formation where the initial conditions for massive star formation are still kept, and to provide insight to the formation of massive stars.

Due to angular resolution limitations, only recently has the study of fragmentation in starless/prestellar cores made significant progress. Lately, a number of studies toward massive star-forming regions with high angular resolutions using interferometers have begun to reveal fragmentation in massive starless cores on 0.1 pc scale (Bontemps et al. 2010; Palau et al. 2013). These studies mostly focus on the massive star-forming sites associated with Infrared Dark Clouds (IRDCs), which are typically at a distance of few kilo-parsecs. We chose Orion as our target region. At a distance of 414 pc (Menten et al. 2007), Orion is the closest active star-forming region that contains massive stars (e.g., Hillenbrand 1997; Hillenbrand & Hartmann

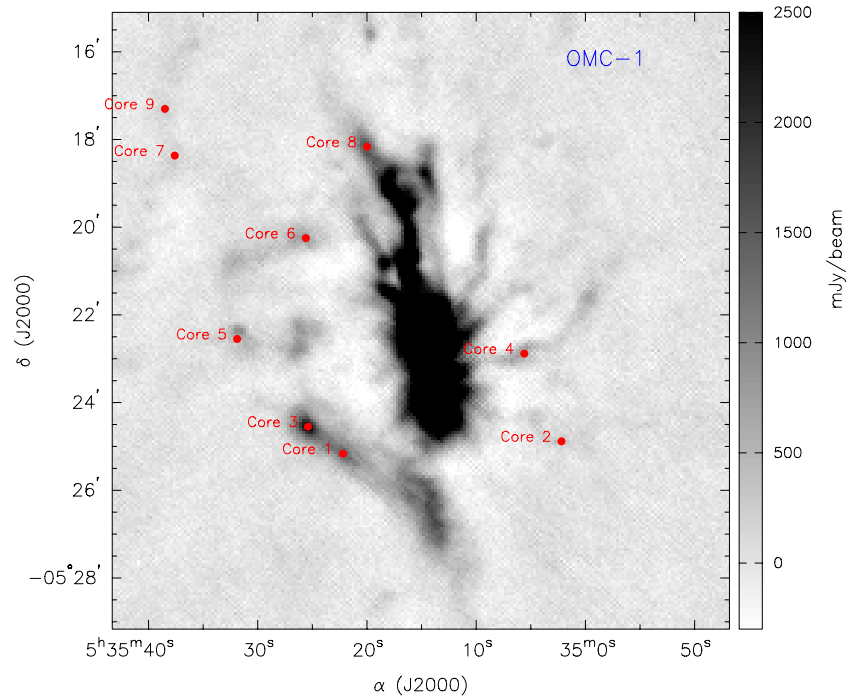


Figure 1. The 850 μm dust continuum image of Orion A-North from the JCMT SCUBA archive. The positions of the nine cores detected with the IRAM 30 m telescope are plotted with red circles.

(A color version of this figure is available in the online journal.)

1998; Johnstone & Bally 1999) as well as massive starless cores (e.g., Nutter & Ward-Thompson 2007; Di Francesco et al. 2008; Sadavoy et al. 2010). It provides an excellent opportunity to study the initial conditions for massive star formation.

2. OBSERVATIONS AND DATA REDUCTION

To fully investigate the substructure and kinematics of starless cores, we observed with the IRAM 30 m single dish telescope and the Combined Array for Research in Millimeter-wavelength (CARMA) interferometer. Although we observed multiple molecular line tracers, CS(2–1) is mainly used for the analysis. CS(2–1) is used extensively as a tracer for high-density gas. Although previous studies indicated that C-bearing species may be depleted during the prestellar phase (e.g., Taylor et al. 1998), several studies have also suggested that associated C-bearing molecules have not been frozen out at the very early stage of star formation.

2.1. The Sample

Our sample of starless cores were chosen from Nutter & Ward-Thompson (2007). They conducted a large survey in Orion at 850 μm dust continuum with the Submillimetre Common User Bolometer Array (SCUBA). By comparing the survey with the *Spitzer* IRAC catalog, the study provided a complete catalog of prestellar cores and protostellar cores down to the lower completeness limit at $\sim 0.3 M_{\odot}$ in the Orion A North, A South, Orion B North, and B South regions. We chose 16 prestellar cores from the catalog with dust masses⁴ ranging from $1 M_{\odot}$ to $50 M_{\odot}$ and observed them with the IRAM 30 m telescope. The reason to include a few cores with low dust mass estimates was to compare them with massive cores; surprisingly, some cores with

Table 1
Coordinates of the IRAM 30 m Detected Sources

Source	R.A.(2000)	Decl.(2000)	850 μm Dust Mass ^a
Core 1	05:35:22.2	−05:25:10	47.4 M_{\odot}
Core 2	05:35:02.2	−05:24:53	1.4 M_{\odot}
Core 3	05:35:25.4	−05:24:33	54.6 M_{\odot}
Core 4	05:35:05.6	−05:22:53	8.5 M_{\odot}
Core 5	05:35:31.9	−05:22:33	5.3 M_{\odot}
Core 6	05:35:25.6	−05:20:15	14.0 M_{\odot}
Core 7	05:35:37.6	−05:18:22	5.8 M_{\odot}
Core 8	05:35:20.0	−05:18:10	12.5 M_{\odot}
Core 9	05:35:38.5	−05:17:18	3.0 M_{\odot}

Note. ^a The 850 μm dust masses were calculated assuming a temperature of 20 K, a mass opacity of $0.01 \text{ cm}^2 \text{ g}^{-1}$, and a distance of 414 pc to Orion. See Nutter & Ward-Thompson (2007) for more details.

low dust mass estimates turned out have large gas mass estimates from our observations (see Section 3.1.2). Of the 16 sources in the IRAM 30 m sample, nine were detected in at least one molecular line tracer. Figure 1 shows the positions of the nine detected cores, and Table 1 lists the coordinates and the masses calculated from the 850 μm dust continuum observations of those cores. Table 2 lists the coordinates of the non-detected sources. The CARMA observations were performed toward eight of the nine starless cores that had been detected with the IRAM observations.

The cores are mostly located in the filamentary structures around the periphery of the central Orion Molecular Cloud 1 (OMC-1). Core 1 and Core 3 are in the Orion Bar photon-dominated region (PDR; e.g., Lis & Schilke 2003). Core 2 and Core 4 are associated with the “radiating filaments” (Johnstone & Bally 1999) from OMC-1 of which the formation mechanisms are still unclear (Myers 2009). In particular, Core 4 is close to the Orion BN/KL region which is observed with

⁴ The term “dust mass” used in this paper refers to a total mass from dust and gas derived from dust emission by assuming a gas-to-dust ratio (typically 100).

Table 2
Coordinates of Non-detected Sources

Source Name ^a	R.A.(2000)	Decl.(2000)
OrionAN-535031-52140	05:35:03.1	−05:21:40
OrionAN-535354-52130	05:35:35.4	−05:21:30
OrionAN-535181-52129	05:35:18.1	−05:21:29
OrionAN-535040-52046	05:35:04.0	−05:20:46
OrionAN-535146-51847	05:35:14.6	−05:18:47
OrionAN-535376-51822	05:35:37.6	−05:18:22
OrionAN-535200-51810	05:35:20.0	−05:18:10
OrionAN-535385-51718	05:35:38.5	−05:17:18
OrionAN-535217-51312	05:35:21.7	−05:13:12
OrionAN-535255-50237	05:35:25.5	−05:02:37
OrionAN-535207-50053	05:35:20.7	−05:00:53

Note. ^a The source names are quoted from Nutter & Ward-Thompson (2007).

powerful outflows and “H₂ fingers” (Zapata et al. 2009; Peng et al. 2012); however, the location of Core 4 is in a larger spatial scale structure and is not associated with the HH bullets or H₂ fingers (Buckle et al. 2012). Core 7 and Core 9 are associated with a filament north-east to OMC-1, which has been suggested as a PDR (Shimajiri et al. 2013, in preparation).

2.2. IRAM 30 m Observations

The observations were performed in 2010 August toward the 16 starless cores in Orion. The heterodyne receiver EMIR was used. The bands E090, E150, and E230 in combination captured various lines. The bands E090 and E150 were used to perform the molecular line observations with CS(2–1) at 97.980968 GHz, C³⁴S(2–1) at 96.41298 GHz and CS(3–2) at 146.96905 GHz. We used VESPA as the spectral back-end with a spectral resolution of 40 kHz (~ 0.06 km s^{−1} at 3 mm) and a total bandwidth of 80 MHz. On-the-fly mapping was performed with both horizontal and vertical scanning to span an area of about 2′ by 2′ for each source. The observations were performed in position-switching mode with off-position at 05^h36^m15^s.0, −05°02′34″ (Ikeda et al. 2007). Calibration scans were taken about every 15 minutes. The pointing was checked every two hours. The beam size (full-width half-power) is $\sim 25''.5$ at the frequency of CS(2–1) and C³⁴S(2–1), and 17″ at the frequency of CS(3–2). The beam efficiency⁵ is 81% for CS(2–1) and C³⁴S(2–1), and 74% for CS(3–2).

The data reduction was done with the CLASS package from the GILDAS⁶ software. All the data are re-gridded to have at least three pixels in one beam size. All 16 sources were

⁵ See <http://www.iram.es/IRAMES/mainWiki/Iram30mEfficiencies>

⁶ See <http://www.iram.fr/IRAMFR/GILDAS/>

Table 4
Sensitivity Limits from the IRAM and CARMA Observations

Source	IRAM CS(2–1)	IRAM CS(3–2)	IRAM C ³⁴ S(2–1)	CARMA CS(2–1)
Core 1	0.24 K	0.67 K	0.18 K	0.15 Jy beam ^{−1}
Core 2	0.15 K	0.66 K	0.34 K	0.11 Jy beam ^{−1}
Core 3	0.10 K	0.54 K	0.23 K	0.20 Jy beam ^{−1}
Core 4	0.085 K	0.20 Jy beam ^{−1}
Core 5	0.10 K	0.41 K	0.18 K	0.11 Jy beam ^{−1}
Core 6	0.09 K	0.15 Jy beam ^{−1}
Core 7	0.075 K	0.16 Jy beam ^{−1}
Core 8	0.1 K	0.75 K	0.32 K	0.18 Jy beam ^{−1}
Core 9	0.075 K

observed with CS(2–1) and ¹²CO(2–1); only nine of which showed detections (Table 3).

2.3. CARMA Observations

CARMA is a heterogeneous array combining three types of antenna: six 10 m antennas, nine 6 m antennas and eight 3.5 m antennas. The data presented in this paper used the cross-correlated data from the 10 m antennas and the 6 m antennas. The CARMA observations were performed toward eight starless cores (from the nine sources detected by the IRAM 30 m telescope) between 2010 May and 2011 November. Only one source (Core 8) out of the eight observed sources was observed with both the D and E array configuration, and the remaining seven cores were observed with only the D array. The data presented in this paper focus on CS(2–1) at 97.98096 GHz, with one band for N₂H⁺(1–0) at 93.17383 GHz and one band for the continuum observation. The projected baselines of the D array range from 11 m to 150 m, providing sensitivity to spatial scales up to $\sim 30''$ and a synthesized beam of $\sim 5''$ at 3 mm. The E array has the projected baselines ranging from 8 m to 66 m, providing sensitivity to spatial scales up to $\sim 40''$ and a synthesized beam of $\sim 7''$ at 3 mm. The spectral resolutions are 0.15 km s^{−1} for Cores 1, 2, 4, and 5, and 0.06 km s^{−1} for Cores 3, 6, 7, and 8. The amplitude calibration is estimated to be 10%, and the uncertainties discussed afterward are only statistical, not systematic. All the data reduction were done with the MIRIAD software (Sault et al. 1995).

The sensitivity limits of all the data present from IRAM and CARMA in this paper are summarized in Table 4.

2.4. Herschel and JCMT Archival Data

For the eight, sources observed by CARMA, we also present the 500 μ m images from the *Herschel* archival data as well as the

Table 3
Molecular Line Observations with the IRAM 30 m Telescope

Line Transition	Frequency (GHz)	Signal-to-Noise Ratio (from the Peak Intensity)								
		Core 1	Core 2	Core 3	Core 4	Core 5	Core 6	Core 7	Core 8	Core 9
H ¹³ CO ⁺ (1–0)	86.754330	X	X	X	...	X
C ³⁴ S(2–1)	96.412982	8.0	5.3	13.4	...	4.7	...	X	10.6	X
CS(2–1)	97.980968	28.0	13.1	43.3	96.2	37.0	5.6	70.2	137.9	28.7
¹⁸ CO(1–0)	109.782182	7.7	6.5	10.9	18.5	...
CS(3–2)	146.969049	20.0	8.0	36.0	...	12.3	...	7.1	20.8	X
N ₂ D ⁺ (2–1)	154.217206	X	X	X	...	X
¹⁸ CO(2–1)	219.560319	5.7	3.3	9.8	6.8	...
¹² CO(2–1)	230.537990	13.7	X	11.5	20.8	4.7	52.3	55.6	92.8	50.0

Notes. “X” means no detection (below the 3 σ level) with the molecular line. “...” means the molecular line was not observed.

Table 5
Velocity Ranges for the IRAM 0th Moment Maps

Source	CS(2–1) (km s ^{−1})	CS(3–2) (km s ^{−1})	C ³⁴ S(2–1) (km s ^{−1})
Core 1	11.91–9.16	12.35–8.88	11.04–9.44
Core 2	13.23–6.77	12.23–6.93	11.35–8.84
Core 3	11.73–8.57	12.23–8.25	11.04–9.24
Core 4	12.03–5.58
Core 5	8.57–4.38	8.25–4.86	8.45–7.45
Core 6	8.39–5.04
Core 7	11.91–6.77
Core 8	11.91–7.49	12.00–6.83	12.24–8.45
Core 9	12.15–7.37

850 μm image from the James Clerk Maxwell telescope (JCMT) archival data. The *Herschel* 500 μm image is downloaded from the Herschel Science Archive⁷. The data were taken in 2009 September with the Spectral and Photometric Imaging Receiver. The observation identifier number is 1342184386, and the data presented in this paper is calibrated to level 2. The 850 μm image from JCMT SCUBA-2 is downloaded from the site of public processed data in the JCMT Science Archive⁸. The project number is M09BI121 and the data was taken in 2010 February.

3. RESULTS AND DATA ANALYSIS I: MORPHOLOGY AND PROPERTIES

3.1. IRAM Maps

3.1.1. CS(2–1), CS(3–2) and C³⁴S

We detected nine out of the 16 cores in the IRAM 30 m sample. We assessed the *Spitzer* 8.0 μm maps and the IRAM CO data (C¹²O(2–1), C¹⁸(2–1)) and confirmed that these are indeed starless cores that lack detected infrared counterparts and outflows. To determine the spatial extent of each core, we examined the data cube and selected the velocity range to make 0th moment maps based on 3σ levels in channel maps. We then defined a projected core as the lowest closed contour in 0th moment maps over that range (Figure 2) and masked based on that contour. The velocity ranges used for 0th moment maps of CS(2–1), CS(3–2), and C³⁴S(2–1) are summarized in Table 5; the range is the 3σ detection range of molecular emission in the defined core. The defined cores have high signal-to-noise ratio⁹ in the 0th moment maps, implying that the cores are likely surrounded by large-scale emission. While this large-scale emission will have some effect on our core properties (e.g., fluxes, masses), it is difficult to disentangle the contributions.

We note that Cores 1, 7, and 8 are associated with ambient extended structures and no closed contours can be determined. For these three cores, masking is performed based on the lowest contour that shows distinct structures different than the extended structures. Although in general the morphology and sizes of our gas derived cores are consistent with the 850 μm dust continuum

emission derived cores (Nutter & Ward-Thompson 2007), there are some clear discrepancies (e.g., Cores 5 and 7) that could suggest that the dust and gas traced by CS(2–1) are not well correlated in the early stage of star formation, which is also seen in other studies (Morata et al. 2012).

The IRAM CS(2–1) sources are mostly single-peaked (Figure 2), and are usually associated with non-spherical, elongated structures. The non-spherical morphologies agree with previous studies of dense cores, which showed that the majority of dense cores are tri-axial including prolate or oblate (e.g., Tassis 2007). For five of the cores, we can compare the CS(3–2) and C³⁴S(2–1) emission with the CS(2–1) emission (Figure 3), and the 0th moment images are mapped using the full range of the lines. CS(3–2) and C³⁴S(2–1) are in general optically thinner than CS(2–1). These three lines show consistent morphologies, and the CS(3–2) peaks well coincide with the CS(2–1) peaks. There are a few differences; for example, the C³⁴S(2–1) emission shows more than one peak for Core 2, but shows only one peak for Core 8. Both CS(3–2) and C³⁴S show more spherical shape of the core than the CS(2–1) emission.

H¹³CO⁺(1–0) and N₂D⁺(2–1) are not detected toward any core (Table 3). A classification between “early-time” and “late-time” molecules have been suggested by several studies based on the time at which these molecules reached their peak abundance (e.g., Taylor et al. 1998; Morata et al. 2003). CS(2–1) is in general classified as an “early-time” tracer while H¹³CO⁺(1–0) and nitrogen-bearing species are “late-time” tracers (e.g., Morata et al. 2005). Therefore, the detection of CS(2–1) and the non-detections of H¹³CO⁺(1–0) and N₂D⁺(2–1) in Cores 1, 2, 3, and 5 suggest that the cores are in the very early stage of the evolution and are chemically young, before the depletion of CS(2–1) becomes significant (e.g., Tafalla et al. 2002). However, the detail of the chemistry depends on various models (e.g., Vasyunina et al. 2012).

3.1.2. CS(2–1) Column Densities

As we have IRAM 30 m CS(2–1) and C³⁴S(2–1) emission for five of the cores, we are able to estimate their optical depths and peak column densities. We first calculate the optical depths of CS(2–1) and C³⁴S(2–1) by

$$\frac{T_{\text{MB}}(\text{C}^{34}\text{S})}{T_{\text{MB}}(\text{CS})} = \frac{1 - \exp(-\tau)}{1 - \exp(-\tau f)}, \quad (1)$$

where T_{MB} is the main beam temperature of the molecular line, and f is the CS to C³⁴S ratio. T_{MB} is calculated from the observed antenna temperature divided by the main beam efficiency (0.8 as reported in Section 2.2). $T_{\text{MB}}(\text{CS})$ and $T_{\text{MB}}(\text{C}^{34}\text{S})$ are measured from the flux within the beam size centered at the CS(2–1) peak emission. The measured values for $T_{\text{MB}}(\text{CS})$ and $T_{\text{MB}}(\text{C}^{34}\text{S})$ are listed in Table 6. We use a terrestrial value of 22.5 for the CS to C³⁴S ratio (e.g., Kameya et al. 1986). We further estimate the excitation temperature from the radiative transfer equation

$$T_{\text{ex}} = \frac{h\nu}{k} \left[\ln \left(\frac{h\nu/k}{\frac{T_{\text{MB}}}{1 - e^{-\tau}} + J_{\nu}(T_{\text{bg}})} + 1 \right) \right]^{-1},$$

where $J_{\nu}(T) = ((h\nu/k)/(e^{h\nu/kT} - 1))$, ν is the frequency of the molecular transition, and T_{bg} is the background temperature assumed to be 2.73 K. With the assumption of LTE, the column

⁷ See http://herschel.esac.esa.int/Science_Archive.shtml

⁸ See <http://www.cadc.hia.nrc.gc.ca/jcmt/search/product/>

⁹ The noises on 0th moment maps were calculated with $\sigma_I = \sigma_T N_{\text{ch}}^{1/2} \Delta\nu$, where σ_I is the noise on 0th moment maps, σ_T is the noise on channel maps, $N_{\text{ch}}^{1/2}$ is the number of channels in the summed velocity range, and $\Delta\nu$ is the channel width.

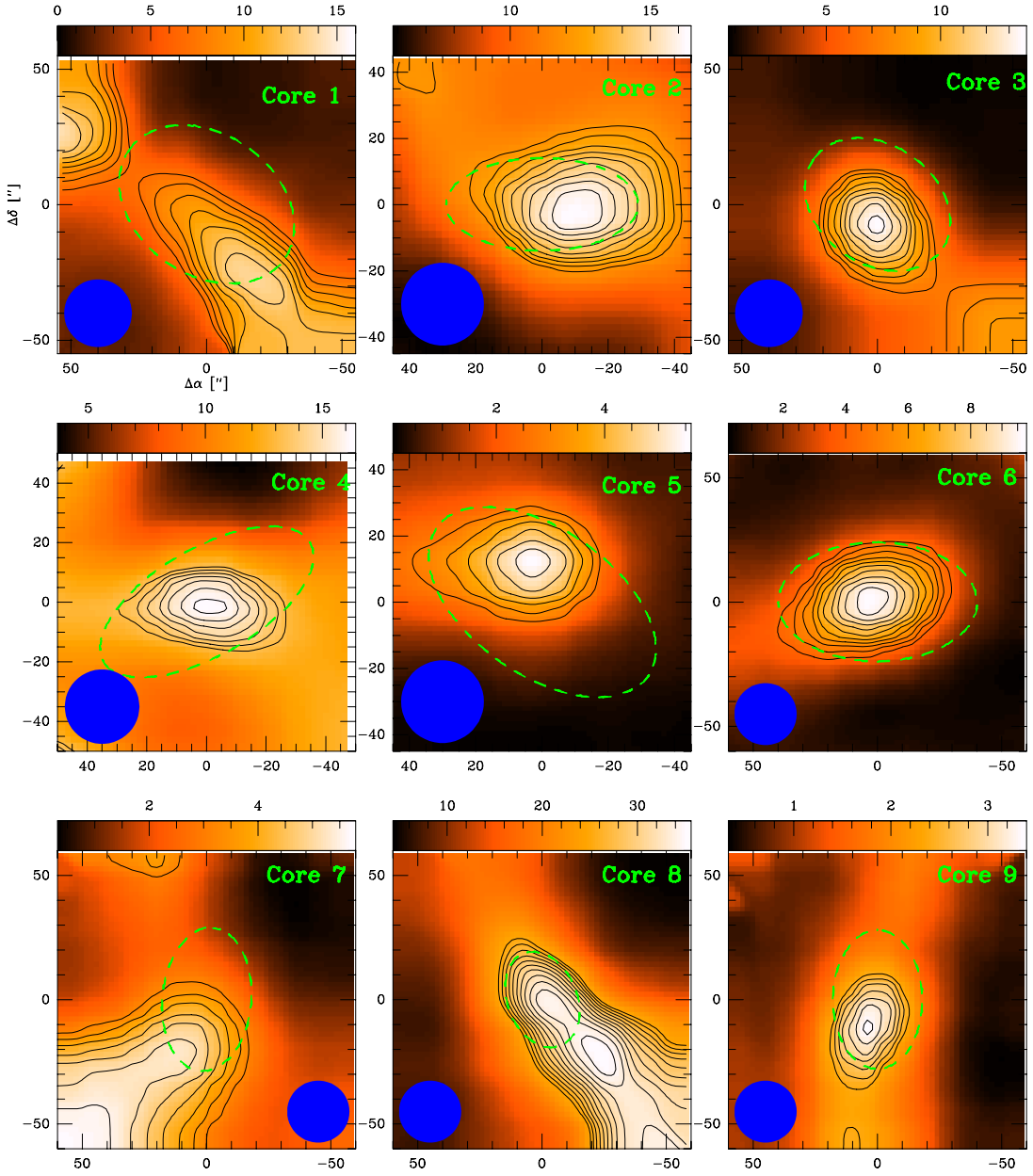


Figure 2. The 0th moment maps from the IRAM CS(2–1) observations toward the nine starless cores. The blue circle in each panel indicates the beam size (25'') of the IRAM 30 m telescope. The green dashed ellipses are the definitions of 850 μm dust cores from Nutter & Ward-Thompson (2007). Most of the cores show single peaks and are associated with elongated structures. The contour levels (σ , starting level, interval) are as following: Core 1: $\sigma = 0.1 \text{ K km s}^{-1}$, 70σ , 10σ ; Core 2: $\sigma = 0.1 \text{ K km s}^{-1}$, 120σ , 5σ ; Core 3: $\sigma = 0.04 \text{ K km s}^{-1}$, 175σ , 20σ ; Core 4: $\sigma = 0.05 \text{ K km s}^{-1}$, 265σ , 10σ ; Core 5: $\sigma = 0.05 \text{ K km s}^{-1}$, 55σ , 10σ ; Core 6: $\sigma = 0.04 \text{ K km s}^{-1}$, 100σ , 15σ ; Core 7: $\sigma = 0.04 \text{ K km s}^{-1}$, 80σ , 10σ ; Core 8: $\sigma = 0.05 \text{ K km s}^{-1}$, 500σ , 20σ ; Core 9: $\sigma = 0.04 \text{ K km s}^{-1}$, 60σ , 4σ .

(A color version of this figure is available in the online journal.)

Table 6
Properties of the Five Cores with CS(2–1) and C³⁴S(2–1) IRAM 30 m Detections

Source	Transition	T_A (K)	τ	$\int T_A dv$ (K km s ^{−1})	$T_{\text{ex,CS(2-1)}}$ (K)	N_{H_2} ($\times 10^{23} \text{ cm}^{-2}$)	Σ_{H_2} (g cm ^{−2})	M_{H_2} (M_\odot)	n_{H_2} ($\times 10^6 \text{ cm}^{-3}$)
Core 1	CS(2–1)	6.81	2.24	12.46 ± 0.1	12.76	7.28 ± 0.06	1.81 ± 0.01	26.60 ± 0.15	5.44 ± 0.03
	C ³⁴ S(2–1)	0.72	0.10						
Core 2	CS(2–1)	3.90	2.69	15.74 ± 0.1	8.38	10.02 ± 0.06	2.48 ± 0.01	36.60 ± 0.15	7.47 ± 0.03
	C ³⁴ S(2–1)	0.47	0.12						
Core 3	CS(2–1)	5.32	3.66	10.67 ± 0.04	10.02	8.85 ± 0.03	2.19 ± 0.01	32.34 ± 0.15	6.61 ± 0.03
	C ³⁴ S(2–1)	0.82	0.16						
Core 5	CS(2–1)	2.64	4.78	4.63 ± 0.05	6.42	5.32 ± 0.06	1.32 ± 0.01	19.40 ± 0.15	3.97 ± 0.03
	C ³⁴ S(2–1)	0.51	0.21						
Core 8	CS(2–1)	12.47	4.69	31.88 ± 0.05	19.01	42.14 ± 0.07	10.45 ± 0.02	154.00 ± 0.3	31.46 ± 0.06
	C ³⁴ S(2–1)	2.37	0.21						

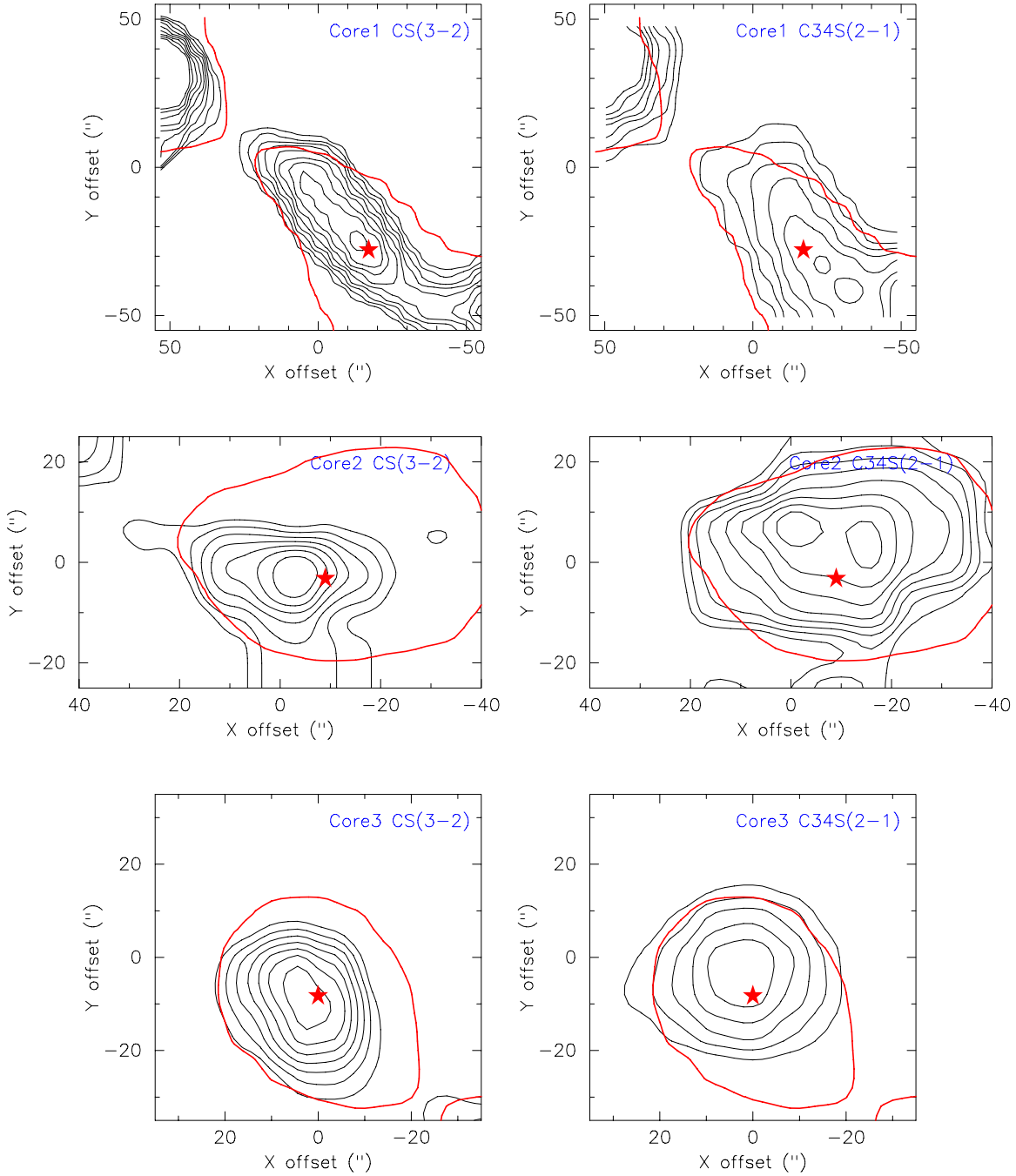


Figure 3. The 0th moment maps from the IRAM CS(3–2) and C³⁴S(2–1) observations for the five starless cores. The black contours in the left panels show CS(3–2) and the black contours in the right panels show C³⁴S(2–1). The red contours are the IRAM CS(2–1) emission (lowest contours in Figure 2) and the red stars are where the CS(2–1) emission peak. The contour levels (σ , starting level, interval) for CS(3–2) are: Core 1: $\sigma = 0.25$ K km s^{−1}, 40 σ , 5 σ ; Core 2: $\sigma = 0.30$ K km s^{−1}, 34 σ , 2 σ ; Core 3: $\sigma = 0.22$ K km s^{−1}, 50 σ , 10 σ ; Core 5: $\sigma = 0.15$ K km s^{−1}, 25 σ , 5 σ ; Core 8: $\sigma = 0.34$ K km s^{−1}, 50 σ , 10 σ . The contour levels (σ , starting level, interval) for C³⁴S(2–1) are: Core 1: $\sigma = 0.07$ K km s^{−1}, 8 σ , 2 σ ; Core 2: $\sigma = 0.16$ K km s^{−1}, 8 σ , 0.5 σ ; Core 3: $\sigma = 0.1$ K km s^{−1}, 10 σ , 2 σ ; Core 5: $\sigma = 0.06$ K km s^{−1}, 5 σ , 2 σ ; Core 8: $\sigma = 0.16$ K km s^{−1}, 15 σ , 5 σ .

(A color version of this figure is available in the online journal.)

density can be derived

$$\begin{aligned} \left[\frac{N}{\text{cm}^{-2}} \right] &= 1.67 \times 10^{14} \frac{Q_{\text{rot}}}{g_k g_l} \left[\frac{S_{JKI}}{\text{erg cm}^3 \text{ statC}^{-2} \text{ cm}^{-2}} \right]^{-1} \\ &\times \left[\frac{\mu}{D} \right]^{-2} e^{E_u/T_{\text{ex}}} \left[\frac{\nu}{\text{GHz}} \right]^{-1} \frac{J_v(T_{\text{ex}})}{J_v(T_{\text{ex}}) - J_v(T_{\text{bg}})} \\ &\times \frac{\tau}{1 - e^{-\tau}} \left[\frac{\int T_{\text{MB}} dv}{\text{K km s}^{-1}} \right]. \end{aligned}$$

The parameters used in the equation are listed in Table 7 (Rohlfs & Wilson 2000). We assume an abundance ratio between CS(2–1) and H₂ at the center of a core to be 2×10^{-10} (the result from modeling in a later section) in converting the CS column densities to H₂ column densities. Using a constant abundance ratio instead of a profile with central depletion is justified since the cores are chemically less evolved (see Section 3.1.1). Frau et al. (2010) reported similar CS-to-H₂ abundance ratio (few times 10^{-10}) in the chemically young starless cores in the pipe nebula.

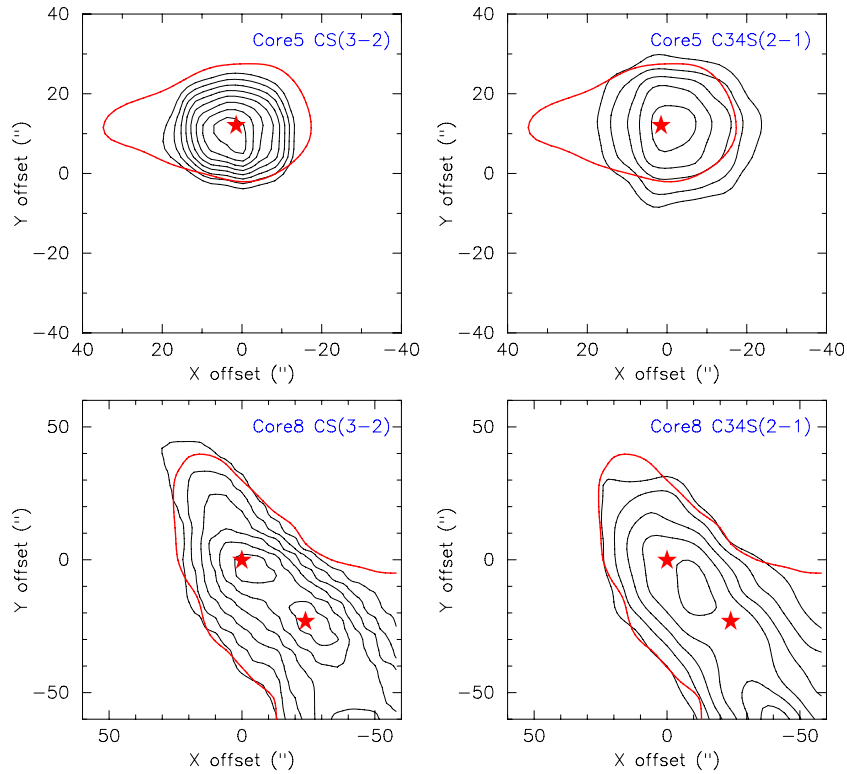


Figure 3. (Continued)

Table 7
CS(2–1) Properties

Parameter	Description	Value
Q_{rot}	Rotational partition function	$0.86T_{\text{ex}}$
g_l, g_k	Degeneration of the quantum number	$g_l = 1, g_k = 1$
$S\mu^2$	S: line strength, μ^2 : dipole moment	7.71 debye
E_u	Energy in the upper state	7.0 K
ν	Frequency of the molecular line	97.980968 GHz

We further estimate the masses and number densities within the beam ($25''$) for the core peak assuming sphericity:

$$M_{\text{H}_2} = \mu m_{\text{H}} D^2 \int N_{\text{H}_2} d\Omega,$$

$$n_{\text{H}_2} = \frac{M_{\text{H}_2}}{4\pi r^3/3},$$

where m_{H} is the hydrogen mass, D is the distance to Orion (414 pc from Menten et al. (2007)), and r is the beam radius. The derived values for the optical depths, excitation temperatures, column densities, and LTE masses at the peak positions are listed in Table 6.

The optical depths of CS(2–1) are between 2 to 5; similar optical depths for CS(2–1) are reported in other star-forming cores (Frau et al. 2010; Morata et al. 2003). The excitation temperatures range from 6.5 K to 19 K with the average temperature of 11.3 K, in agreement with the kinetic temperature of 10 K (to 15 K) for starless cores (e.g., Schnee et al. 2009). This suggests that the cores are thermalized; the thermalization is also suggested by the high number density (several times 10^6 cm^{-3}) compared to the critical density for CS ($\sim 10^5 \text{ cm}^{-3}$; see Evans (1999)). The LTE masses indicate that these cores

are massive star-forming regions. However, the LTE masses are inconsistent with the dust mass estimates from the $850 \mu\text{m}$ observations, possibly due to the higher temperature (20 K) used in the dust masses calculation, the assumed dust opacity, the imperfect coupling between dust and gas, and optical depth effects. Also, due to the large-scale emission surrounding the cores, the masses here may be overestimated.

The derived column densities ($\geq 10^{23} \text{ cm}^{-2}$) are comparable to several massive star-forming regions (e.g., Beuther et al. 2007) and are slightly higher than some intermediate mass-star forming regions (e.g., Lee et al. 2011). The number densities range from 4.7×10^6 to $3.7 \times 10^7 \text{ cm}^{-3}$. The simulation performed by Keto & Field (2005) which includes hydrodynamics, radiative cooling, variable molecular abundance, and radiative transfer concludes that starless cores with central densities larger than a few times 10^5 cm^{-3} are dynamically unstable and may proceed to gravitational collapse, suggesting that our cores are gravitationally bound.

3.2. CARMA Maps

3.2.1. CARMA CS(2–1) Maps

Of the nine cores detected by the IRAM 30 m, eight of them were followed up by higher resolution CARMA observations (Figure 4). Most of the cores (except Core 5) show multiple intensity peaks in the CARMA CS(2–1) emission within the single peaked IRAM cores, suggesting fragmentation. These fragments are not in spherical morphologies and are spatially connected to each other. The number of fragments range from three to five in each core. Core 5 is associated with one single object in spherical shape and does not show signs of fragmentation.

The CARMA CS(2–1) emission well traces the small-scale filamentary structures probed by the JCMT SCUBA-2 $850 \mu\text{m}$

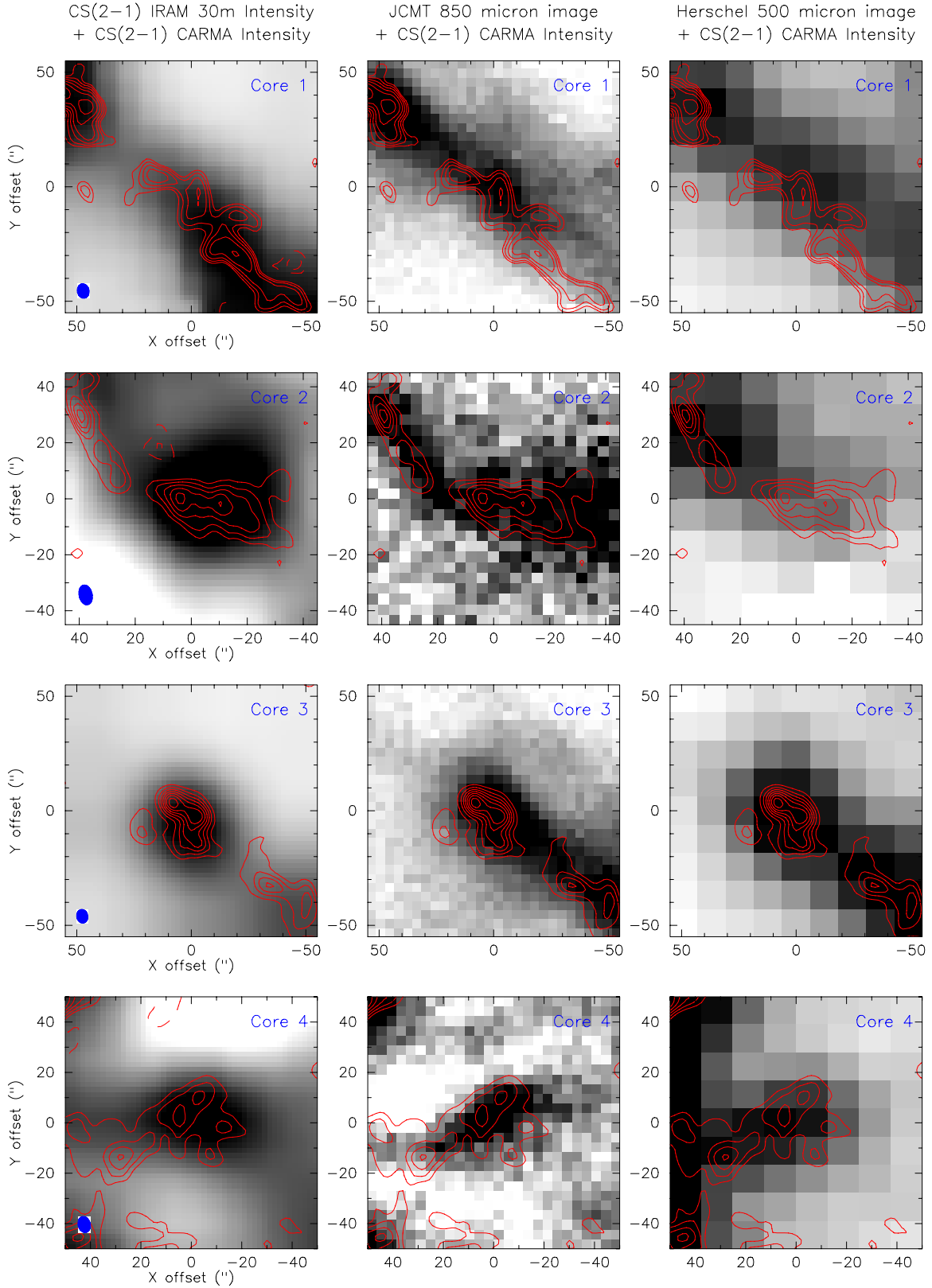


Figure 4. The 0th moment maps from the CARMA CS(2-1) observations (red contours) overlaid on the IRAM CS(2-1) observations (first column), JCMT 850 μm dust continuum (second column), and the *Herschel* 500 μm dust continuum (third column). The contour levels (σ , starting level, interval) are: Core 1: $\sigma = 0.32 \text{ Jy beam}^{-1} \text{ km s}^{-1}$, $\pm 5\sigma$, $\times \sqrt{2}\sigma$; Core 2: $\sigma = 0.32 \text{ Jy beam}^{-1} \text{ km s}^{-1}$, $\pm 5\sigma$, $\pm 2\sigma$; Core 3: $\sigma = 0.45 \text{ Jy beam}^{-1} \text{ km s}^{-1}$, $\pm 5\sigma$, $\pm 5\sigma$; Core 4: $\sigma = 0.4 \text{ Jy beam}^{-1} \text{ km s}^{-1}$, $\pm 5\sigma$, $\pm 3\sigma$; Core 5: $\sigma = 0.18 \text{ Jy beam}^{-1} \text{ km s}^{-1}$, $\pm 5\sigma$, $\pm 5\sigma$; Core 6: $\sigma = 0.16 \text{ Jy beam}^{-1} \text{ km s}^{-1}$, $\pm 10\sigma$, $\pm 10\sigma$; Core 7: $\sigma = 0.2 \text{ Jy beam}^{-1} \text{ km s}^{-1}$, $\pm 5\sigma$, $\pm 2\sigma$; Core 8: $\sigma = 0.6 \text{ Jy beam}^{-1} \text{ km s}^{-1}$, $\pm 10\sigma$, $\pm 3\sigma$.

(A color version of this figure is available in the online journal.)

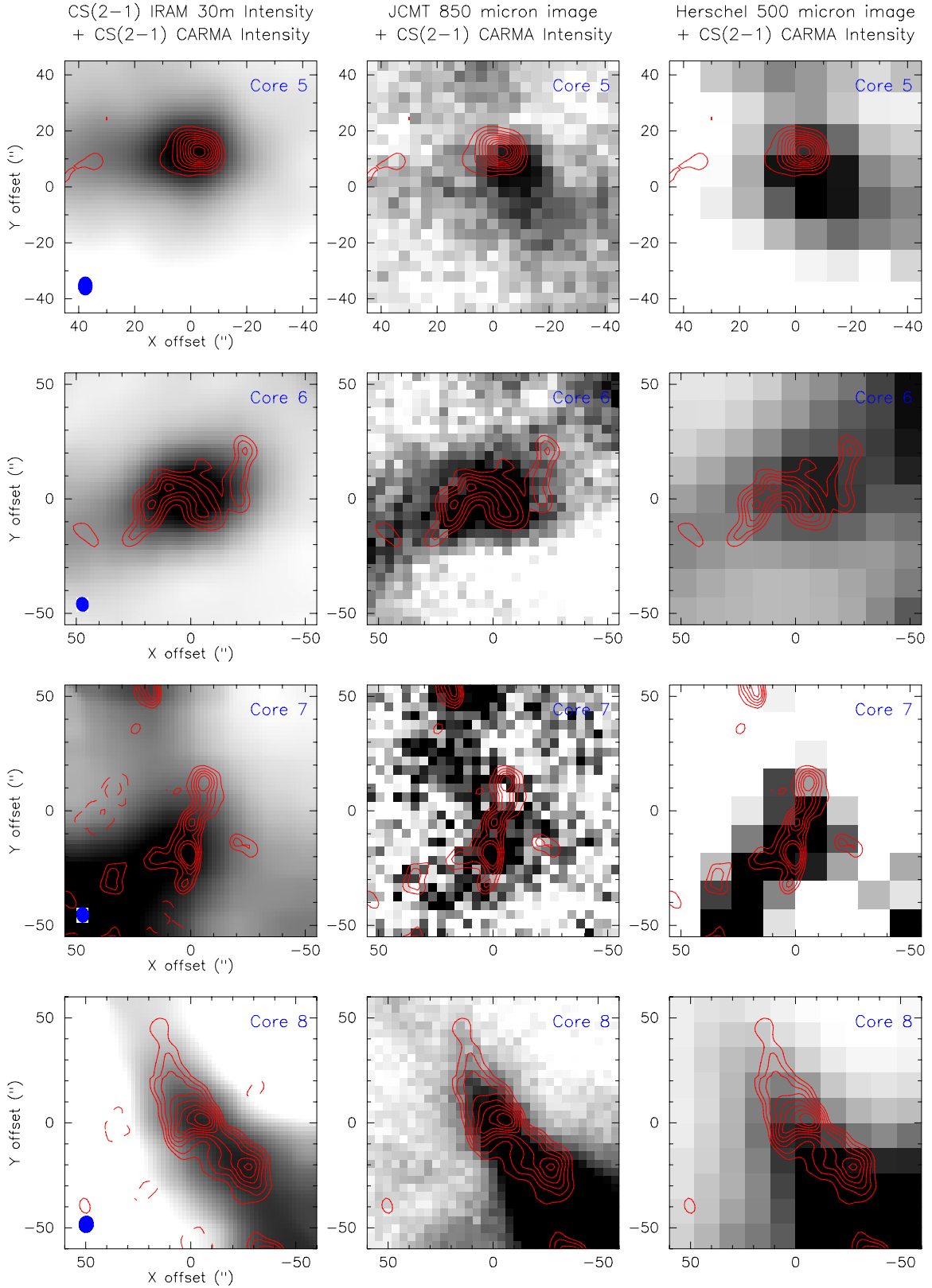


Figure 4. (Continued)

observations and *Herschel* 500 μm observations. For example, Core 1 is associated with the filamentary structure in the north-east and south-west direction as clearly seen in the 850 μm and 500 μm images. The tight connection between the structures probed by CS(2-1) and dust emission is reminiscent of the star

formation activities along filamentary structures at large scales (see Lee et al. 2012), suggesting the importance of filamentary structures to star formation at small scales.

We compare the CS(2-1) fluxes from the IRAM observations and the CARMA observations for all eight cores (Figure 5).

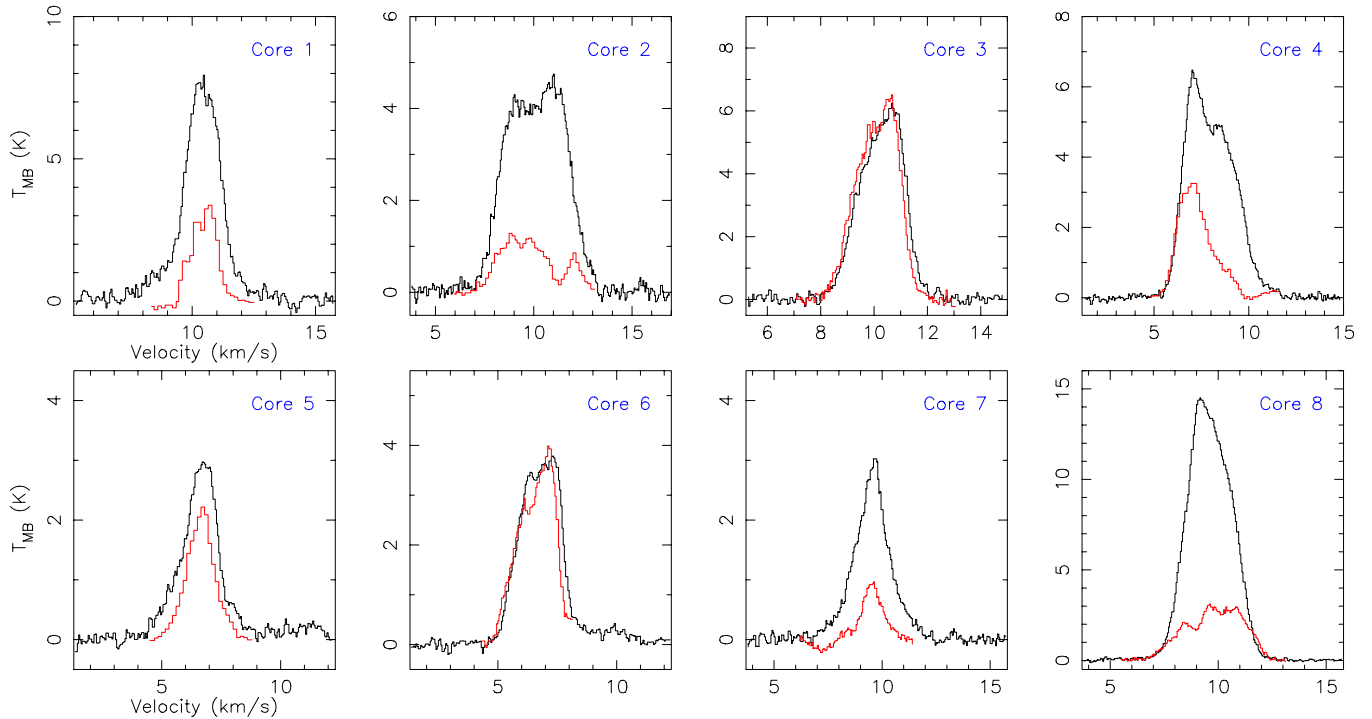


Figure 5. Comparison between the IRAM CS(2–1) flux density (black lines) and the CARMA CS(2–1) flux (red lines). The rms noises for the IRAM data are: 0.24 K (Core 1), 0.15 K (Core 2), 0.1 K (Core 3), 0.085 K (Core 4), 0.1 K (Core 5), 0.09 K (Core 6), 0.075 K (Core 7), and 0.075 K (Core 8). The rms noises for the convolved CARMA data are: 0.096 K (Core 1), 0.17 K (Core 2), 0.17 K (Core 3), 0.094 K (Core 4), 0.087 K (Core 5), 0.093 K (Core 6), 0.116 K (Core 7), 0.122 K (Core 8).

(A color version of this figure is available in the online journal.)

For this comparison, the CARMA maps are convolved with the beam size of the IRAM 30 m telescope (25"). For both IRAM and CARMA fluxes, the spectra are then extracted from the averaged flux within the lowest contour level for each core shown in Figure 3. Some of the cores (Cores 1, 2, 4, 7, and 8) show that the CARMA fluxes are largely resolved out while the other cores (Cores 3, 5, and 6) show comparable CARMA and IRAM fluxes. The largely resolved out fluxes with Core 1, 2, 4, and 8 may be associated with converging flows at larger scales (see Section 4.1.3).

3.2.2. CARMA $N_2H^+(1-0)$ Maps

$N_2H^+(1-0)$ is detected only in Core 4 and Core 8 with CARMA while the other cores show no detections (Figure 6). For Core 4, $N_2H^+(1-0)$ shows multiple peaks with the strongest emission outside the IRAM contour. For Core 8, $N_2H^+(1-0)$ also shows two major peaks. Although the positions of $N_2H^+(1-0)$ peaks do not well coincide with the CS(2–1) peaks for both cores, $N_2H^+(1-0)$ still shows the clumpy nature for these cores, suggesting that the fragmentation detected by optically thicker tracer CS(2–1) is not due to the chemical effect from depletion.

3.2.3. CARMA Continuum Maps at 3 mm

There was no detection in the CARMA continuum at 3 mm. The non-detection is reminiscent of the lack of 3 mm continuum emission in CARMA D array maps toward nine starless cores in the Perseus molecular cloud (Schnee et al. 2010). Lee et al. (2012) suggested that the non-detections in the Perseus sample are probably due to a combination of resolving-out structure and sensitivity. Future observations with better sensitivity are required for further characterization on dust properties

Table 8
Noise Level for 3 mm Continuum Observations and Mass Sensitivity

Source	Noise (mJy beam ⁻¹)	Mass ^a (M_\odot)
Core 1	4.7	<2.85
Core 2	1.3	<0.79
Core 3	7.7	<4.67
Core 4	1.9	<1.15
Core 5	2.2	<1.33
Core 6	2.4	<1.42
Core 7	15.0	<9.09
Core 8	1.9	<1.15

Note. ^a The mass corresponds to the 3σ upper limit for detection of small-scale structure.

at millimeter-wavelengths. We calculated the mass sensitivity from the 3σ upper limit using the equation:

$$M = \frac{d^2 S_{3\text{mm}}}{B_\nu(T_D) \kappa_{3\text{mm}}} \quad (2)$$

where d is distance to Orion, $S_{3\text{mm}}$ is three times the noise level, B_ν is the Planck function as a function of dust temperature T_D , and $\kappa_{3\text{mm}}$ is the dust opacity. We use a typical dust temperature of 10 K for starless cores and $0.00169 \text{ cm}^2 \text{ g}^{-1}$ for $\kappa_{3\text{mm}}$ (an extrapolated value from Ossenkopf & Henning 1994) by assuming a gas-to-dust ratio of 100 and $\beta = 2$. The noise levels for the cores and the mass upper limits corresponding to 3σ are presented in Table 8. These mass limits are only for substructures and the large-scale emission is not detected.

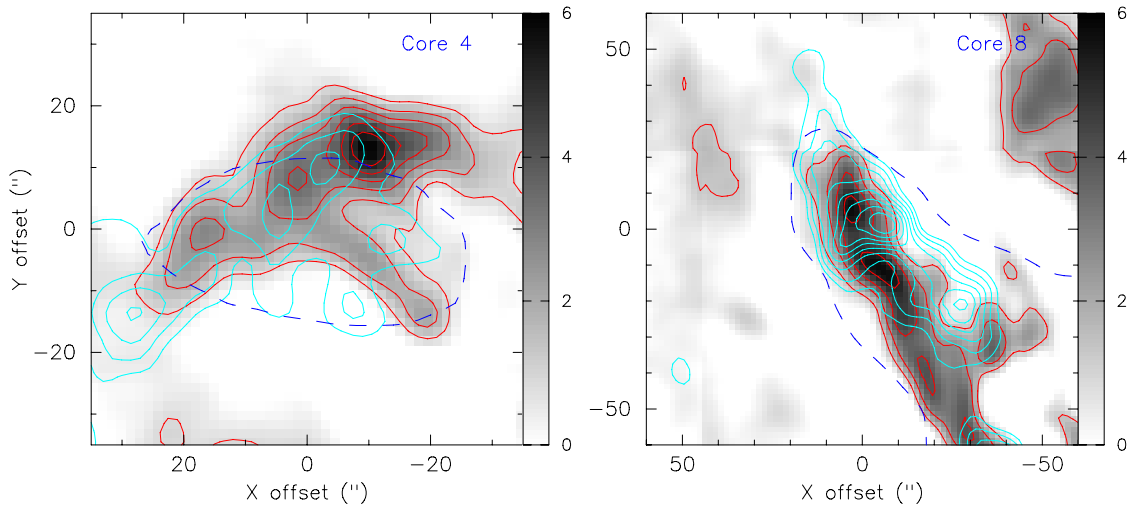


Figure 6. The 0th moment maps from the CARMA $\text{N}_2\text{H}^+(1-0)$ observation (red contours and gray scale) in comparison with the 0th moment maps from the CARMA CS(2–1) observations (cyan contours). The blue dashed lines are the IRAM CS(2–1) contour. The contour levels for the $\text{N}_2\text{H}^+(1-0)$ emission are 10%, 20%, 30%, 40%, 50%, 60%, 70%, 80%, 90%, and 100% of the peak intensities (in $\text{Jy beam}^{-1} \text{ km s}^{-1}$).

(A color version of this figure is available in the online journal.)

Table 9
2D Fitting of Velocity Gradients

Source	v_0 (km s^{-1})	a ($\text{km s}^{-1} \text{ pc}^{-1}$)	b ($\text{km s}^{-1} \text{ pc}^{-1}$)	g ($\text{km s}^{-1} \text{ pc}^{-1}$)	θ_g (degree)
Core 1	10.49 ± 0.20	3.43 ± 0.35	1.17 ± 0.43	4.28 ± 0.42	71.9 ± 5.7
Core 2	9.91 ± 0.16	-9.96 ± 0.51	-6.91 ± 0.76	14.31 ± 0.71	55.2 ± 2.8
Core 3	10.25 ± 0.20	0.87 ± 0.45	-1.11 ± 0.41	1.66 ± 0.51	321.7 ± 17.3
Core 4	7.98 ± 0.19	-8.87 ± 0.52	-1.76 ± 0.92	10.67 ± 0.64	78.79 ± 3.4
Core 5	7.28 ± 0.19	-4.31 ± 0.84	-8.07 ± 1.40	10.81 ± 1.52	28.10 ± 8.1
Core 6	7.07 ± 0.12	-0.43 ± 0.45	-1.36 ± 0.58	1.69 ± 0.61	17.42 ± 22.9
Core 7	9.77 ± 0.20	2.67 ± 0.46	6.73 ± 0.48	8.54 ± 0.55	21.63 ± 3.8
Core 8	9.45 ± 0.10	-6.01 ± 0.34	0.18 ± 0.31	7.09 ± 0.40	271.8 ± 3.2
Core 9	9.29 ± 0.28	3.68 ± 0.80	3.77 ± 0.58	6.22 ± 0.83	44.3 ± 7.6

4. RESULTS AND DATA ANALYSIS II: KINEMATICS

4.1. Large-scale Kinematics with IRAM

4.1.1. Velocity Gradients Fitting

Figure 7 shows the first moment maps from the IRAM CS(2–1) data for the nine cores, masked based on the CS(2–1) contours. Velocity gradients are observed in several cores (Cores 1, 2, 4, 7, 8, and 9). To derive the magnitudes of the velocity gradients, we assume that the gradients are linear in both right ascension and declination. Using the first-moment maps, the velocity gradients are computed based on the method described in Goodman et al. (1993), but with the MPFIT function (Markwardt 2009) implemented in IDL performing the least-square fitting:

$$v_{LSR} = v_0 + a\Delta\alpha + b\Delta\delta, \quad (3)$$

where v_0 is the systematic velocity, a and b are the velocity gradients along the right ascension and declination, and $\Delta\alpha$ and $\Delta\delta$ are the position offsets. The total velocity gradients are defined as

$$g = \frac{\sqrt{a^2 + b^2}}{D},$$

where D is the distance (414 pc for Orion). The direction of the velocity gradients is then defined as $\theta_g = \tan^{-1}(b/a)$.

The fitting results of the velocity gradients for all nine cores are listed in Table 9. The total velocity gradients range from 1.4 to 12.1 $\text{km s}^{-1} \text{ pc}^{-1}$, with an average value of 6.2 $\text{km s}^{-1} \text{ pc}^{-1}$. Most of the velocity gradients are large compared to dense cores including starless cores and protostars (0.3 to 4 $\text{km s}^{-1} \text{ pc}^{-1}$ from Goodman et al. (1993) and 0.5 to 6 $\text{km s}^{-1} \text{ pc}^{-1}$ in Caselli et al. (2002)). Recent observations with higher resolutions have found larger velocity gradients. For example, Curtis & Richer (2011) found the velocity gradients of $\sim 5.5 \text{ km s}^{-1} \text{ pc}^{-1}$ for starless cores and $\sim 6 \text{ km s}^{-1} \text{ pc}^{-1}$ for protostars in Perseus. Also, Tobin et al. (2011) found a median velocity gradient of 10.7 $\text{km s}^{-1} \text{ pc}^{-1}$ with several Class 0 objects from interferometric data.

These velocity gradients are often interpreted as rotation. However, the common interpretation of rotation needs to be treated with caution since an inflowing filament can also produce the velocity patterns that mimic rotation (Tobin et al. 2012). Infall and rotation in spherical objects are easy to distinguish since spherical infall exhibits blue-skewed spectra with optically thick lines across the object (e.g., Lee et al. 1999; Pavlyuchenkov et al. 2008). However, infall and rotation in filaments are more difficult to disentangle as both generate velocity gradients. The spectral maps and position–velocity (P – V) diagrams need to be examined carefully to correctly interpret the kinematics.

4.1.2. Spectral Maps

Cores 1, 2, 4, and 8 have the most prominent velocity gradients in the IRAM 30 m data. By using a linear cut

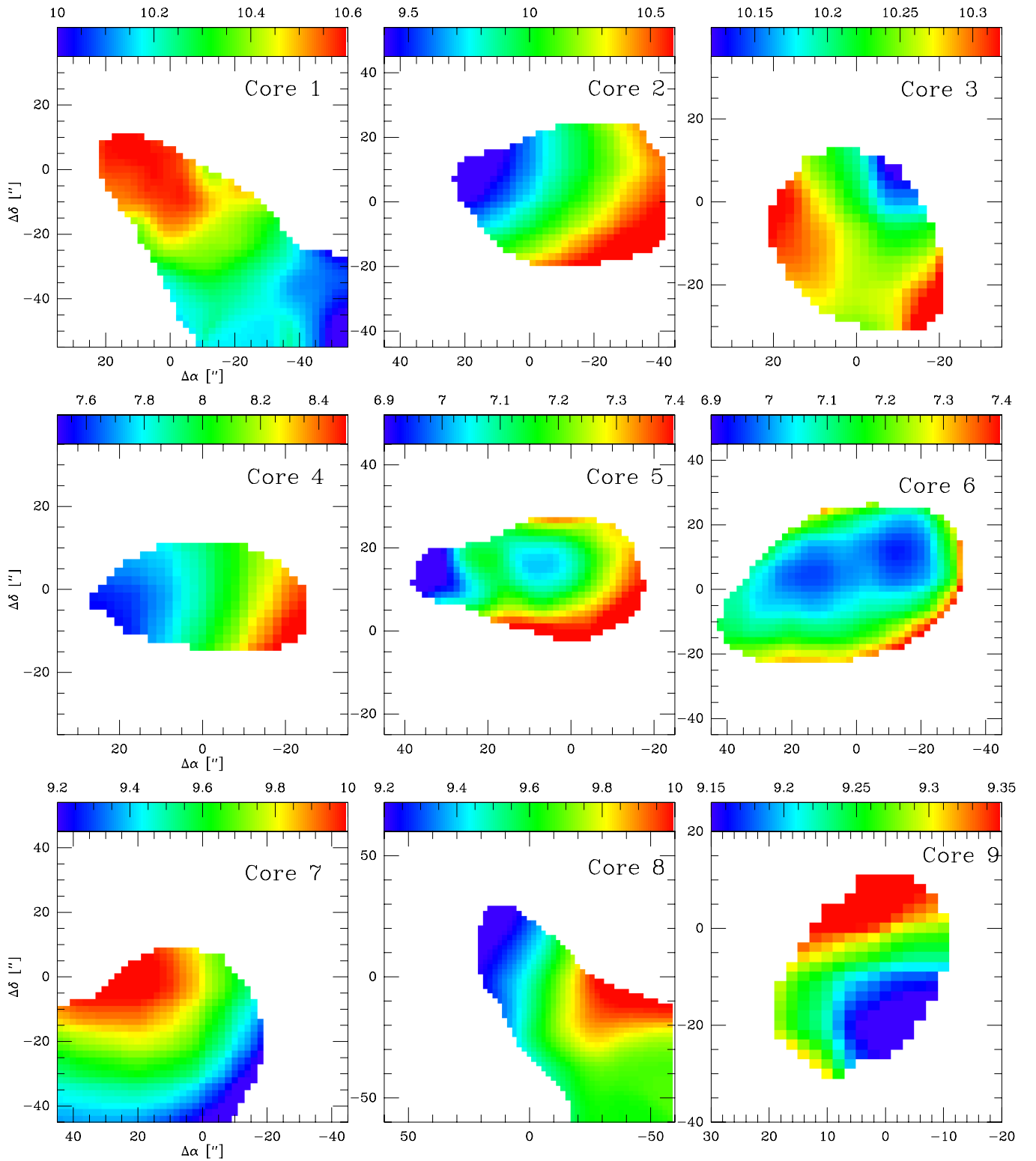


Figure 7. First moment maps from the IRAM CS(2–1) data. The color scale indicates velocity in km s^{-1} .

(A color version of this figure is available in the online journal.)

across the minimum and maximum velocities in the maps, one notices two main features of the spectra across these cores (Figure 8). First, a gradual shift from blue to red in the peak velocities is observed across the cores. The separations between the blue-shifted and red-shifted peak velocities are $\sim 0.8 \text{ km s}^{-1}$ (Core 1), 2.5 km s^{-1} (Core 2), 1.6 km s^{-1} (Core 4), and 1.7 km s^{-1} (Core 8). Also, The velocity peaks

of the blue components and that of the red components do not vary significantly across the cores, suggesting that the gas flows at a nearly constant speed. Second, the blue components have stronger intensities than the red components. These two features are observed for all four cores. To explain these two features, we performed a radiative transfer modeling of Core 2.

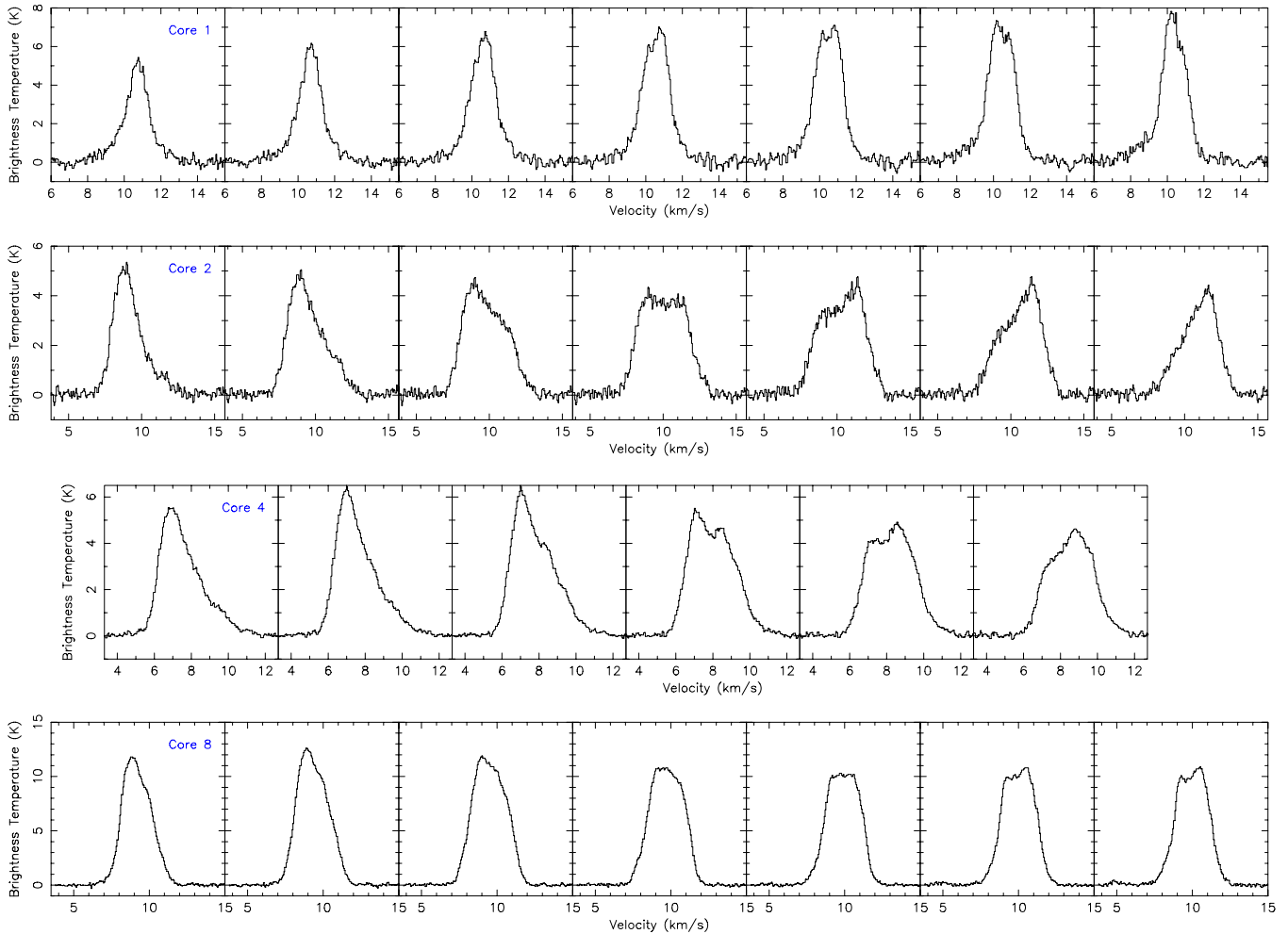


Figure 8. Spectra of the four cores along the directions of the velocity gradients.
(A color version of this figure is available in the online journal.)

4.1.3. Radiative Transfer Modeling

We compare the CS(2–1) spectra from Core 2 with radiative transfer calculations performed with the code LIME (Line Modeling Engine; Brinch & Hogerheijde 2010). We chose Core 2 to model since it best presents the two common features observed for the four cores. The code calculates the emergent spectra by solving the molecular line excitation with 3D Delaunay grids for photon transport and accelerated Lambda Iteration for population calculations. The inputs to the code, which are based on 3D structures, are the density, temperature, chemical abundance, velocity, and linewidth profiles. Users also control parameters such as molecular lines, inclination angles, dust properties, and image resolutions.

To be consistent with the flattened morphologies of the cores, we consider a cylindrically symmetric filament that contains inflowing¹⁰ gas from the two sides to the center with an inclination angle (Figure 9), which is similar to filament models (e.g., Peretto et al. 2006). The density is considered to vary with the cylindrical R and Z . The density profile has the form of $n(R, Z) = n_0/[1 + (R/R_0)^\alpha]/[1 + (Z/Z_0)^\alpha]$, where n_0 , R_0 and Z_0 are constant. The power-law index α is taken to be 2.5 in the modeling, consistent with other starless cores (Tafalla et al. 2002, 2004). We varied n_0 with 3.0×10^6 , 4.0×10^6 , and

$5.0 \times 10^6 \text{ cm}^{-3}$; R_0 and Z_0 were varied with four sets of numbers respectively: (4180 AU, 17333 AU), (5513 AU, 30000 AU), (6180 AU, 35066 AU), and (10000 AU, 43333 AU).

The temperature is assumed to be a typical temperature of 10 K for starless cores (e.g., Schnee et al. 2009). For the CS(2–1) abundance, we have considered constant abundance ratios $[\text{CS}]/[\text{H}_2] = 10^{-9}$, 3×10^{-10} , 2×10^{-10} and a centrally depleted profile that has the abundance ratio of 10^{-11} in the center and 10^{-9} in the outer envelope. For the velocity field, we have considered two profiles in both the velocity fields that are along the Z -axis only. First, we considered constant velocities including 1.3 km s^{-1} and 1.5 km s^{-1} . Second, we considered a profile that has the form of Keplerian rotation: $v(Z) = v_0(Z/Z_c)^{-0.5}$, where Z_c is a constant to modulate the profile. v_0 was varied with 2.0 km s^{-1} , 3.0 km s^{-1} , and 4.0 km s^{-1} ; Z_c was varied with 500 AU and 2000 AU. The line dispersion was considered with 0.5 km s^{-1} and 0.8 km s^{-1} . The inclination angles were tested with 18 deg, 45 deg, and 60 deg.

The best-fit gives a density profile of $n(R, Z) = 3.0 \times 10^6/[1 + (R/10000 \text{ AU})^{2.5}]/[1 + (Z/43333 \text{ AU})^{2.5}]$, a constant temperature of 10 K, a constant $[\text{CS}]/[\text{H}_2]$ abundance ratio of 2.0×10^{-10} , a constant linewidth of 0.8 km s^{-1} , a constant inflow velocity of 1.5 km s^{-1} , and an inclination angle of 45 deg. The total reduced χ^2 is calculated to be 1.58. The red line in the spectra of Core 2 in Figure 10 shows the best-fit from the radiative transfer modeling. The top figure shows the result from

¹⁰ To distinguish from 1D spherical infall, we use the term “inflow” to describe gas infall on a 2D filament.

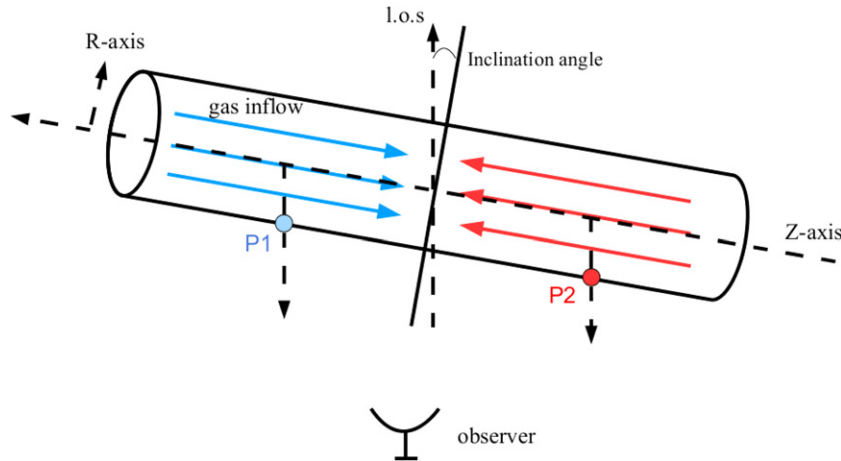


Figure 9. The model for the radiative transfer modeling.
(A color version of this figure is available in the online journal.)

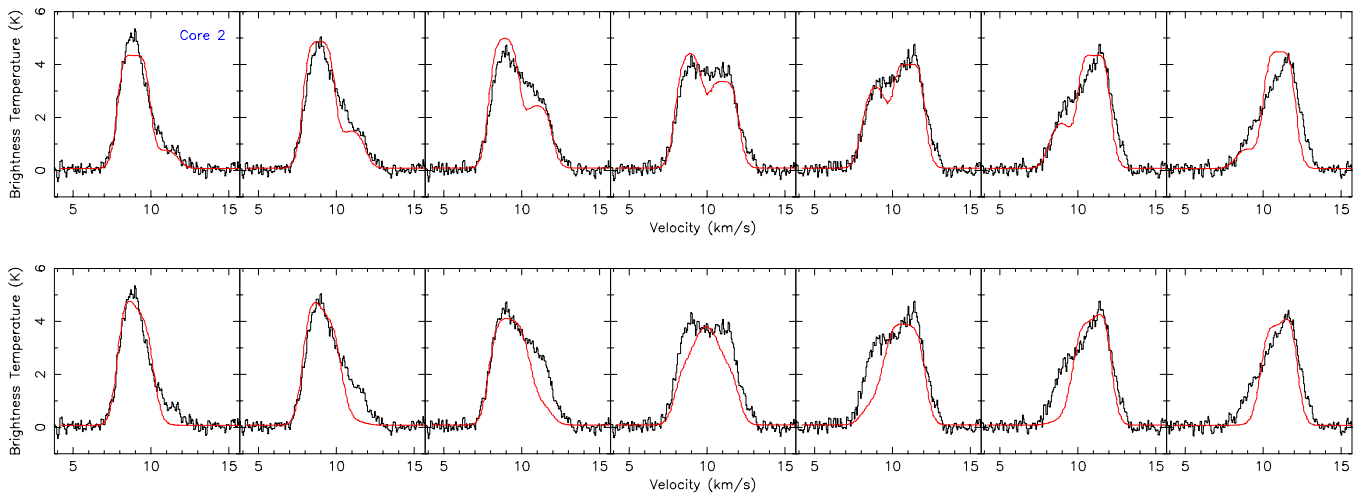


Figure 10. The inflow model (top) and the rotation model (bottom). The black lines are from the data of Core 2 and the red lines indicate the radiative transfer model.
(A color version of this figure is available in the online journal.)

the inflow model. The model has been convolved with the same beam size as the observational data.

The model successfully explains the two features we observed in the spectral maps. With an inclination angle, the gas flow further from observers becomes blue-shifted and the side closer to observers becomes red-shifted. Therefore, shifts of peak velocities from blue to red are observed. For an optically thick line such as CS(2–1), the emission produced in the blue-shifted side is closer to the symmetrical center (P1 in Figure 9) than the emission produced in the red-shifted side due to the projection (P2 in Figure 9). The spectral intensity is higher closer to the symmetric center since the excitation temperature is higher due to the density profile. As a result, we see the intensities in the blue-shifted side larger than the red-shifted side. The reason for this asymmetry is similar to the blue-skewed spectra for spherical infall (e.g., Evans 1999). However, we stress that the central dip seen in the model shown at the center of the core is not caused by self-absorption. Instead, the dip is due to the overlapping between the two Gaussian velocity components. Self-absorption would occur at the inflow velocity for each of the velocity component; however, although CS(2–1) is optically thick ($\tau \sim 3$) for our cores, we do not observe self-absorptions.

As mentioned above, it is considerably challenging to distinguish between 2D inflow or rotation on a filament from observa-

tions (Tobin et al. 2012). To examine the differences between the two compared with our data, we also performed the radiative transfer modeling on a cylindrically symmetric filament with rotation on the R -axis. All the profiles and parameters are the same as the best-fit model for filamentary inflow except for the velocity field. The velocity field we adopted is a constant velocity field along the line-of-sight since the two peaks of the red and blue components nearly stay constant and the best-fit for the inflow model gives a constant velocity. Therefore, the velocity field shows a profile of differential rotation where $\omega(z) \propto (1/z)$.

Figure 10 shows the spectra from the rotation model. The black lines are from the data of Core 2 and the red lines indicate the radiative transfer model. As shown in the figure, the model fails to describe not only the broad linewidth in the central position but also the “wing” features in the off-center positions. The χ^2 for the model is 1.8, larger than the inflow model.

In addition, we compare the P – V diagrams between the observational data, inflow model, and rotation model (Figure 11). With the same angular resolution, the inflow model better demonstrates the observed discontinuity between the two velocity components. The data shows an encounter of two velocity components at the position of zero offset. Such a feature is clearly seen in the inflow model but not in the rotation model at all. In summary, we suggest that the inflow model

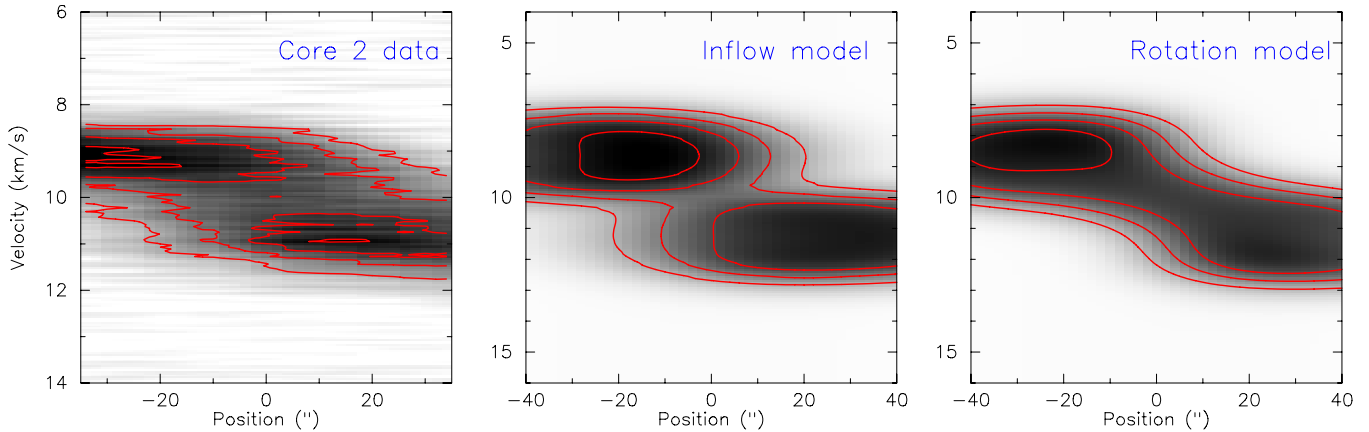


Figure 11. The P - V diagrams of the data (left panel), inflow model (central panel), and rotation model (right panel). The P - V diagrams are from the cut shown in Figure 8. The contours are 30%, 50%, 70%, and 90% of the peak values in all three panels.

(A color version of this figure is available in the online journal.)

best describes the data and is the dominating mechanism for the kinematics.

4.2. Small-scale Kinematics with CARMA

In the higher resolution CARMA maps, the kinematics of the cores is more complex (Figure 12); the interferometer resolves out large-scale structure in most cores or resolves multiple fragments with their own velocity components. Nonetheless, many of the cores, including Cores 1, 2, 3, 4, and 8, show similar global behavior in the velocity patterns as the IRAM CS(2–1) results.

5. DISCUSSION

5.1. Fragmentation: Large and Small Scale

Fragmentation in large-scale molecular clouds (few parsecs) to star-forming cores (0.1 pc) have been observed by previous observations. At parsec-scales, molecular clouds have been extensively observed to fragment into clumps of sub-parsecs (e.g., Onishi et al. 1998; Ikeda et al. 2007; André et al. 2010; Schneider et al. 2010; Hill et al. 2011; Liu et al. 2012). Several studies on the earliest stage of massive to intermediate star formation with high angular resolution (PdBI and SMA) have revealed fragmentation inside sub-parsec clumps to 0.1 pc cores (e.g., Peretto et al. 2006; Zhang et al. 2009; Pillai et al. 2011) at millimeter wavelengths. These studies have important implications to massive star and cluster formation.

Limited by angular resolution and large distance to massive star-forming sites, the study of fragmentation inside 0.1 pc cores did not progress much until recently. With the angular resolution of $5''$ provided by CARMA and the relatively small distance to Orion (414 pc) in this study, the CARMA observations reach a spatial resolution of ~ 2000 AU. Our observations revealed that multiple fragments are associated with each massive starless core of 0.1 pc (Section 3.2.1), suggesting that fragmentation continues to occur at 0.1 pc scales and 0.1 pc cores fragment to even smaller condensations. Recent observations with comparable angular resolutions have reported similar results of fragmentation inside 0.1 pc massive cores at millimeter wavelengths. For example, Bontemps et al. (2010) observed a total of 23 fragments inside five massive dense cores in Cygnus X. Wang et al. (2011) revealed three condensations of 0.01 pc inside two of the 0.1 pc cores in IRDC G28.34-P1. Among the 18 massive dense cores (~ 0.1 pc) that Palau et al.

(2013) studied, $\geq 50\%$ showed ≥ 4 fragments and 30% showed no signs for fragmentation. Furthermore, using an even higher angular resolution of few hundred AU and targeting nearby star-forming region Ophiuchus, Nakamura et al. (2012) and Bourke et al. (2012) unveiled the fragmentation inside low-mass 0.1 pc prestellar cores, suggesting a scenario beyond single collapse even for low-mass stars. Some of these condensations are prestellar in nature (Bontemps et al. 2010; Nakamura et al. 2012), and some of them are protostellar evidenced by outflows (Wang et al. 2011; Naranjo-Romero et al. 2012).

5.2. Mechanism for Fragmentation: Turbulence + Magnetic Fields

The results from the radiative transfer modeling (Section 4.1.3) suggest a highly supersonic linewidth (0.8 km s^{-1}) for Core 2, implying that the environment is highly turbulent and turbulence is playing an important role in fragmentation. Our modeling also showed that signs for fragmentation occur at the colliding point of the convergent flows. This is broadly consistent with the “turbulent fragmentation” scenario (e.g., Klessen et al. 2005; Padoan & Nordlund 2002), in which density fluctuations are generated at small-scales (0.1 pc) when large-scale shocks dissipate, which lead to star-forming cores.

Our results suggest the number of fragments associated with each massive starless core to be ~ 3 –5. This level of fragmentation is consistent with the recent studies of fragmentation inside massive dense cores in Cygnus-X (Bontemps et al. 2010) and the two prestellar cores in ρ -Ophiuchus (Nakamura et al. 2012). However, this number of fragments is not quite consistent with the prediction from several turbulent fragmentation models (e.g., Bonnell et al. 2004; Dobbs et al. 2005; Jappsen et al. 2005) since these models predict a much higher number of fragments. For example, Dobbs et al. (2005) performed purely hydrodynamical numerical simulations of a turbulent core of density structure $\rho \propto r^{-1.5}$ with a initial mass of $30 M_{\odot}$ (comparable to that of our Core 2) and a radius of 0.06 pc. The study found that the core fragments into ~ 20 objects.

The number of fragments can in principle be reduced by radiation feedback (Krumholz et al. 2007) or magnetic fields (Hennebelle et al. 2011). The combination of the two effects work more efficiently in suppressing fragmentation (Commerçon et al. 2011; Myers et al. 2013), with the radiation feedback effectively suppressing the fragmentation in high-density regions (the center of the core) and magnetic fields

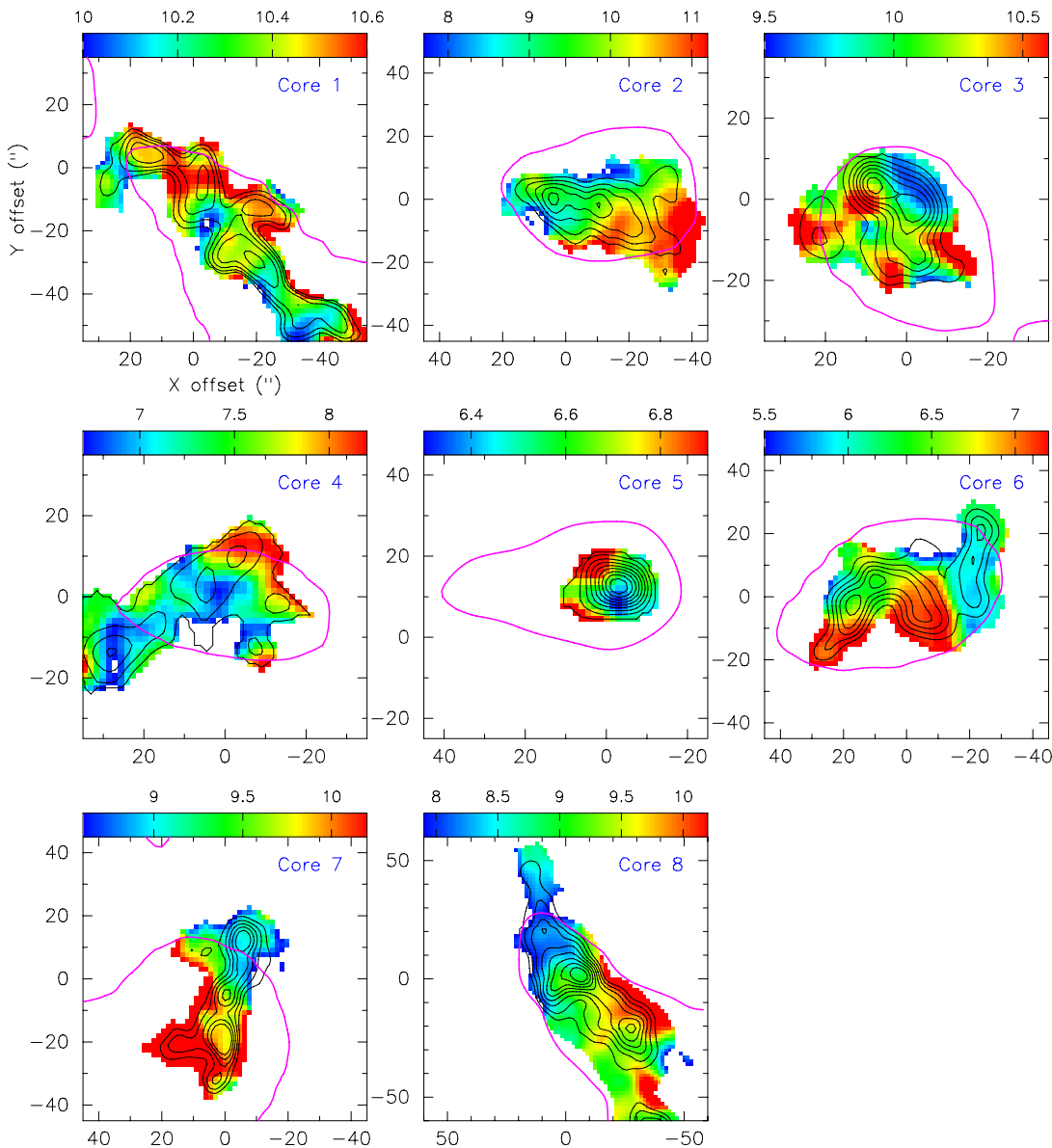


Figure 12. First moment maps from the CARMA CS(2–1) data. The magenta lines are the IRAM CS(2–1) cores. The color indicates velocity in km s^{-1} . The maps are masked based on the 5σ contours in the 0th moment maps (10σ for Cores 6 and 8 to avoid too extended structures).

(A color version of this figure is available in the online journal.)

effectively suppressing the fragmentation in low-density regions (the outer part of the core). However, since the cores we studied are starless, the radiation feedback is expected to be weak. On the other hand, large-scale magnetic fields are observed in the main region of OMC-1 that is close to our cores (e.g., Houde et al. 2004), supporting the argument that magnetic fields may play a role in the fragmentation process. Measurements of magnetic fields on small-scales at the position of the starless cores are needed to further determine the precise role of magnetic fields.

5.3. Role of Supersonic Converging Flows

We obtained a dynamical velocity pattern in the supersonic converging flows (Section 4.1.3) associated with Core 2 from the radiative transfer modeling. Other cores including Cores 1, 4, and 8 all showed similar spectral features as Core 2 (see Section 4.1.2) which can be explained by converging flows. Only a few studies have detected the sign for such supersonic convergent flows at 0.1 pc scale (Csengeri et al. 2011a, 2011b).

The origin of the supersonic flows is difficult to identify; however, it is natural to speculate the origin being the large-scale flows at few parsecs scale since the prominent large-scale filamentary structures may be due to large-scale turbulent flows (e.g., Mac Low & Klessen 2004).

Is the converging flow dynamically important in the star formation process? We calculated the flow crossing time as: $t_{\text{cross}} = R(0.05 \text{ pc})/v_{\text{inf}}(1.5 \text{ km s}^{-1}) = 3.0 \times 10^4 \text{ yr}$, where v_{inf} is the inflow velocity derived from the radiative transfer modeling. The free-fall time is $t_{\text{ff}} = \sqrt{(3\pi/32G\rho)} = 1.5 \times 10^4 \text{ yr}$, where we use the derived central density for ρ in the calculation and therefore the derived free-fall time is an upper limit. The flow-crossing time is the timescale that the flows at 0.1 pc scale bring material down to the center, and the free-fall time is the timescale for the material to collapse gravitationally. The flow crossing time is comparable to the free-fall time, suggesting that the flow is dynamically important in forming the density condensations. However, the crossing time is slightly larger than the free-fall time, suggesting that gravity takes over at

small-scale in driving the dynamical process of star formation. We posit that large-scale flows initiate the density condensations, and gravity becomes dominant at small-scales which enhances the converging flows.

We also estimated the mass inflow rate along an filament: $\dot{M}_{\text{inf}} = 2 \times \pi R_{\text{fil}}^2 \times n_{\text{mean}} \times \mu \times m \times v_{\text{inf}} = 2.35 \times 10^{-3} M_{\odot} \text{ yr}^{-1}$, where $R_{\text{fil}} = 0.025 \text{ pc}$ is the radius of the cylinder (estimated from the model; see Figure 9), n_{mean} is the mean number density of the cylinder, μ is the mean molecular weight, and m is the mass of hydrogen. The LTE mass of Core 2 is estimated to be $36.6 M_{\odot}$ (Section 6), and therefore the formation timescale for Core 2 is $\sim 1.5 \times 10^4 \text{ yr}$. The inflow velocity and mass inflow rate appear to be large compared to low-mass stars which typically have infall velocities $\sim 0.1 \text{ km s}^{-1}$ (e.g., Lee et al. 2004). However, higher inflow velocities and mass inflow rates are not surprising for massive star-forming regions. For example, several high infrared extinction clouds with massive star formation in Rygl et al. (2013) have the spherical infall velocities in the order of $0.3\text{--}7 \text{ km s}^{-1}$ and mass infall rates on the order of $1.4\text{--}22.0 \times 10^{-3} M_{\odot} \text{ yr}^{-1}$. Peretto et al. (2006) reported a similar mass inflow rate in a protocluster NGC 2264-C with intermediate- to high-mass star formation. The study found a mass inflow velocity of 1.3 km s^{-1} along a cylinder-like, filamentary structure on a spatial scale of 0.5 pc . We are probably seeing the continuation of the 0.5 pc scale flow down to the scale of 0.1 pc . However, the underlying physical reason for such highly supersonic velocities is still unclear.

5.4. Implications for Massive Star and Cluster Formation

Our result does not fully support either the turbulent core scenario or the competitive accretion scenario. The discovery of fragments in our study makes it harder to form massive stars in these cores via the turbulent core model proposed by McKee & Tan (2003), since the core mass will eventually go to a number of objects rather than a single star. McKee & Tan (2003) suggest a minimum mass accretion rate of $10^{-3} M_{\odot} \text{ yr}^{-1}$ to overcome the radiation pressure and form a massive star. By this criterion, our Core 2 has a high enough inflow rate to form massive stars; however, the inflow may not feed just one single object since the core contains multiple fragments. Krumholz & McKee (2008) suggest that a minimum column density of 1 g cm^{-2} can avoid fragmentation through radiative feedback. We suggest that this is a necessary but not sufficient condition for massive star formation: all cores in this study have column densities larger than that threshold (see Table 6), and yet they have already fragmented before the radiative feedback kicks in.

Our result is broadly consistent with a scenario of turbulent fragmentation, with the number of fragments perhaps reduced by magnetic fields. However, while it is possible that the fragmentation continues to occur during the later stages of evolution and/or future massive stars could form via competitive accretion (Bonnell et al. 2004; Bonnell & Bate 2006), our observations highlighted a feature that is not present in the standard competitive accretion scenario: rapid converging flows along dense filaments that feed matter into the central region. This feature is similar in spirit to the model proposed by Wang et al. (2010) where the mass accretion rate onto a massive star is set mainly by the large-scale converging or collapsing flow, rather than the gravitational pull of the star itself.

As each fragment has the potential to collapse individually and form protostars, it is suggestive that we are witnessing the formation of clusters at the very early stages and multiplicity occurs already in the prestellar phase. Given a 30% core

formation efficiency (Bontemps et al. 2010) for a $30 M_{\odot}$ core (Section 6), each individual fragment inside a core will be forming low- to intermediate-mass stars. Therefore, we suggest that these cores are in the dynamical state of forming low- to intermediate-mass protoclusters (e.g., Lee et al. 2011).

Although our study is unique in observing massive starless cores at a distance $\leq 500 \text{ pc}$ with high spatial resolution, the number of observed fragments may increase with higher resolution and more sensitivity. Follow-up studies of dust continuum with higher resolution are necessary to compliment this study and accurately constrain the properties of these cores, including the masses and the dynamical states of these cores.

6. CONCLUSION

We observed nine starless cores in the Orion-A North region with the IRAM 30 m telescope and eight cores out of the nine cores with CARMA using CS(2–1). Our main conclusions are as follows:

1. The IRAM 30 m observations showed no detection of $\text{N}_2\text{D}^+(2-1)$ for all the nine cores, and the CARMA observations showed $\text{N}_2\text{H}^+(1-0)$ for only two cores (Core 4 and Core 8). As CS(2–1) is regarded as an “early-time tracer” and N-bearing species ($\text{N}_2\text{D}^+(2-1)$, $\text{N}_2\text{H}^+(1-0)$) as “late-time tracers,” this result suggests that most of our cores are at the very early stage of star formation.
2. The CS(2–1) observations with the IRAM 30 m telescope showed that majority of the starless cores are single-peaked, and the morphologies traced by CS(2–1), $\text{C}^{34}\text{S}(2-1)$, and CS(3–2) are mostly consistent with each other. The column densities estimated from CS(2–1) range from $7\text{--}42 \times 10^{23} \text{ cm}^{-2}$ and the LTE masses range from $20 M_{\odot}$ to $154 M_{\odot}$.
3. The comparison between the CARMA CS(2–1) data, the IRAM CS(2–1) data, JCMT $850 \mu\text{m}$ dust continuum, *Herschel* $500 \mu\text{m}$ data shows that gas structures probed by CS(2–1) are forming along small-scale filamentary structures traced by dust continuum, suggesting the importance of filamentary structures to star formation even at small scales.
4. The CARMA CS(2–1) observations show fragmentation inside all the cores except for Core 5. The number of fragments associated with each core ranges from 3 to 5.
5. Five cores showed obvious velocity gradients across the cores in the IRAM CS(2–1) data. We performed a two-dimensional fitting to the velocity gradients by assuming the velocity gradients are linear. The fitting results showed that the velocity gradients range from $1.7\text{--}14.3 \text{ km s}^{-1} \text{ pc}^{-1}$.
6. Four cores (Core 1, Core 2, Core 4, and Core 8) showed two common features in their spectra along the direction of the velocity gradients. First, the velocity peak changes from blue-shifted to red-shifted across the cores. Second, the intensity of the blue peak is always stronger than the red peak.
7. We propose a model of a cylindrically symmetric filament with converging inflows from the two sides toward the center to explain the two spectral features. We modeled Core 2 with this proposed kinematic model with the radiative transfer code LIME (Brinch & Hogerheijde 2010), and verified that the kinematic model successfully explains the two features. The best-fit gives a constant supersonic speed of 1.5 km s^{-1} for the flow velocity and a supersonic

linewidth of 0.8 km s^{-1} . A mass inflow rate of $2.35 \times 10^{-3} M_{\odot} \text{ yr}^{-1}$ is inferred from the inflow velocity.

8. The supersonic linewidth from the modeling suggests that the core environment is highly turbulent and the fragmentation revealed by the CARMA observations may be due to turbulent fragmentation. However, the number of fragments is much less than the predictions from turbulent fragmentation models (e.g., Dobbs et al. 2005), indicating that magnetic fields may be playing an important role in reducing the level of fragmentation (Hennebelle et al. 2011).
9. The small-scale converging flow is dynamically important to the formation of the cores and their substructures. We suggest that large-scale flows initiate the density condensations, and gravity becomes dominant at small-scales which enhances the converging flows. Due to the high mass inflow rate, each fragment is likely to collapse individually and form seeds for future protoclusters. Given a core formation efficiency of 30%, we suggest that these cores are in the dynamical state of forming low- to intermediate-mass protoclusters.
10. The fragmentation observed in our cores makes massive star formation via the turbulent core model proposed by McKee & Tan (2003) more difficult. Our result does not fully support the standard competitive accretion model either, since it does not account for our inferred rapid inflow along filaments, which may be an important way of feeding massive protostars.

We thank the anonymous referee for valuable comments that improved this paper. We acknowledge support from the Laboratory for Astronomical Imaging at the University of Illinois. Support for CARMA construction was derived from the states of Illinois, California, and Maryland; the Gordon and Betty Moore Foundation; the Eileen and Kenneth Norris Foundation; Caltech Associates; and the National Science Foundation. Ongoing CARMA development and operations are supported by the National Science Foundation, and by the CARMA partner universities. We also acknowledge the support from the National Radio Astronomy Observatory. The National Radio Astronomy Observatory is a facility of the National Science Foundation operated under cooperative agreement by Associated Universities, Inc. Z. Li acknowledges the support in part by NASA grant NNX10AH30G.

REFERENCES

- André, P., Men'shchikov, A., Bontemps, S., et al. 2010, *A&A*, **518**, L102
- Beuther, H., Leurini, S., Schilke, P., et al. 2007, *A&A*, **466**, 1065
- Bonnell, I. A., & Bate, M. R. 2006, *MNRAS*, **370**, 488
- Bonnell, I. A., Vine, S. G., & Bate, M. R. 2004, *MNRAS*, **349**, 735
- Bontemps, S., Motte, F., Csengeri, T., & Schneider, N. 2010, *A&A*, **524**, A18
- Bourke, T. L., Myers, P. C., Caselli, P., et al. 2012, *ApJ*, **745**, 117
- Brinch, C., & Hogerheijde, M. R. 2010, *A&A*, **523**, A25
- Buckle, J. V., Davis, C. J., Francesco, J. D., et al. 2012, *MNRAS*, **422**, 521
- Caselli, P., Benson, P. J., Myers, P. C., & Tafalla, M. 2002, *ApJ*, **572**, 238
- Commerçon, B., Hennebelle, P., & Henning, T. 2011, *ApJL*, **742**, L9
- Csengeri, T., Bontemps, S., Schneider, N., Motte, F., & Dib, S. 2011a, *A&A*, **527**, A135
- Csengeri, T., Bontemps, S., Schneider, N., et al. 2011b, *ApJL*, **740**, L5
- Curtis, E. I., & Richer, J. S. 2011, *MNRAS*, **410**, 75
- Di Francesco, J., Johnstone, D., Kirk, H., MacKenzie, T., & Ledwosinska, E. 2008, *ApJS*, **175**, 277
- Dobbs, C. L., Bonnell, I. A., & Clark, P. C. 2005, *MNRAS*, **360**, 2
- Evans, N. J., II. 1999, *ARA&A*, **37**, 311
- Frau, P., Girart, J. M., Beltrán, M. T., et al. 2010, *ApJ*, **723**, 1665
- Goodman, A. A., Benson, P. J., Fuller, G. A., & Myers, P. C. 1993, *ApJ*, **406**, 528
- Hennebelle, P., Commerçon, B., Joos, M., et al. 2011, *A&A*, **528**, A72
- Hill, T., Motte, F., Didelon, P., et al. 2011, *A&A*, **533**, A94
- Hillenbrand, L. A. 1997, *AJ*, **113**, 1733
- Hillenbrand, L. A., & Hartmann, L. W. 1998, *ApJ*, **492**, 540
- Houde, M., Dowell, C. D., Hildebrand, R. H., et al. 2004, *ApJ*, **604**, 717
- Ikeda, N., Sunada, K., & Kitamura, Y. 2007, *ApJ*, **665**, 1194
- Jappsen, A.-K., Klessen, R. S., Larson, R. B., Li, Y., & Mac Low, M.-M. 2005, *A&A*, **435**, 611
- Johnstone, D., & Bally, J. 1999, *ApJL*, **510**, L49
- Kameya, O., Hasegawa, T. I., Hirano, N., et al. 1986, *PASJ*, **38**, 793
- Keto, E., & Field, G. 2005, *ApJ*, **635**, 1151
- Klessen, R. S., Ballesteros-Paredes, J., Vázquez-Semadeni, E., & Durán-Rojas, C. 2005, *ApJ*, **620**, 786
- Krumholz, M. R., Klein, R. I., & McKee, C. F. 2007, *ApJ*, **656**, 959
- Krumholz, M. R., & McKee, C. F. 2008, *Natur*, **451**, 1082
- Lada, C. J., & Lada, E. A. 2003, *ARA&A*, **41**, 57
- Lee, C. W., Myers, P. C., & Plume, R. 2004, *ApJS*, **153**, 523
- Lee, C. W., Myers, P. C., & Tafalla, M. 1999, *ApJ*, **526**, 788
- Lee, K., Looney, L., Johnstone, D., & Tobin, J. 2012, *ApJ*, **761**, 171
- Lee, K. I., Looney, L. W., Klein, R., & Wang, S. 2011, *MNRAS*, **415**, 2790
- Lis, D. C., & Schilke, P. 2003, *ApJL*, **597**, L145
- Liu, H. B., Jiménez-Serra, I., Ho, P. T. P., et al. 2012, *ApJ*, **756**, 10
- Mac Low, M.-M., & Klessen, R. S. 2004, *RvMP*, **76**, 125
- Markwardt, C. B. 2009, in ASP Conf. Ser. 411, *Astronomical Data Analysis Software and Systems XVIII*, ed. D. A. Bohlender, D. Durand, & P. Dowler (San Francisco, CA: ASP), 251
- McKee, C. F., & Ostriker, E. C. 2007, *ARA&A*, **45**, 565
- McKee, C. F., & Tan, J. C. 2003, *ApJ*, **585**, 850
- Menten, K. M., Reid, M. J., Forbrich, J., & Brunthaler, A. 2007, *A&A*, **474**, 515
- Morata, O., Girart, J. M., & Estalella, R. 2003, *A&A*, **397**, 181
- Morata, O., Girart, J. M., & Estalella, R. 2005, *A&A*, **435**, 113
- Morata, O., Girart, J. M., Estalella, R., & Garrod, R. T. 2012, *MNRAS*, **425**, 1980
- Myers, A. T., McKee, C. F., Cunningham, A. J., Klein, R. I., & Krumholz, M. R. 2013, *ApJ*, **766**, 97
- Myers, P. C. 2009, *ApJ*, **700**, 1609
- Nakamura, F., Takakuwa, S., & Kawabe, R. 2012, *ApJL*, **758**, L25
- Naranjo-Romero, R., Zapata, L. A., Vázquez-Semadeni, E., et al. 2012, *ApJ*, **757**, 58
- Nutter, D., & Ward-Thompson, D. 2007, *MNRAS*, **374**, 1413
- Onishi, T., Mizuno, A., Kawamura, A., Ogawa, H., & Fukui, Y. 1998, *ApJ*, **502**, 296
- Ossenkopf, V., & Henning, T. 1994, *A&A*, **291**, 943
- Padoan, P., & Nordlund, Å. 2002, *ApJ*, **576**, 870
- Palau, A., Fuente, A., Girart, J. M., et al. 2013, *ApJ*, **762**, 120
- Pavlyuchenkov, Y., Wiebe, D., Shustov, B., et al. 2008, *ApJ*, **689**, 335
- Peng, T.-C., Zapata, L. A., Wyrowski, F., Güsten, R., & Menten, K. M. 2012, *A&A*, **544**, L19
- Peretto, N., André, P., & Belloche, A. 2006, *A&A*, **445**, 979
- Pillai, T., Kauffmann, J., Wyrowski, F., et al. 2011, *A&A*, **530**, A118
- Rohlfs, K., & Wilson, T. L. 2000, *Tools of Radio Astronomy* (New York: Springer)
- Rygl, K. L. J., Wyrowski, F., Schuller, F., & Menten, K. M. 2013, *A&A*, **549**, A5
- Sadavoy, S. I., Di Francesco, J., Bontemps, S., et al. 2010, *ApJ*, **710**, 1247
- Sault, R. J., Teuben, P. J., & Wright, M. C. H. 1995, in ASP Conf. Ser. 77, *Astronomical Data Analysis Software and Systems IV*, ed. R. A. Shaw, H. E. Payne, & J. J. E. Hayes (San Francisco, CA: ASP), 433
- Schnee, S., Enoch, M., Johnstone, D., et al. 2010, *ApJ*, **718**, 306
- Schnee, S., Rosolowsky, E., Foster, J., Enoch, M., & Sargent, A. 2009, *ApJ*, **691**, 1754
- Schneider, N., Csengeri, T., Bontemps, S., et al. 2010, *A&A*, **520**, A49
- Tafalla, M., Myers, P. C., Caselli, P., & Walmsley, C. M. 2004, *A&A*, **416**, 191
- Tafalla, M., Myers, P. C., Caselli, P., Walmsley, C. M., & Comito, C. 2002, *ApJ*, **569**, 815
- Tassis, K. 2007, *MNRAS*, **379**, L50
- Taylor, S. D., Morata, O., & Williams, D. A. 1998, *A&A*, **336**, 309
- Tobin, J. J., Hartmann, L., Bergin, E., et al. 2012, *ApJ*, **748**, 16
- Tobin, J. J., Hartmann, L., Chiang, H.-F., et al. 2011, *ApJ*, **740**, 45
- Vasyunina, T., Vasyunin, A. I., Herbst, E., & Linz, H. 2012, *ApJ*, **751**, 105
- Wang, K., Zhang, Q., Wu, Y., & Zhang, H. 2011, *ApJ*, **735**, 64
- Wang, P., Li, Z.-Y., Abel, T., & Nakamura, F. 2010, *ApJ*, **709**, 27
- Zapata, L. A., Schmid-Burgk, J., Ho, P. T. P., Rodríguez, L. F., & Menten, K. M. 2009, *ApJL*, **704**, L45
- Zhang, Q., Wang, Y., Pillai, T., & Rathborne, J. 2009, *ApJ*, **696**, 268
- Zinnecker, H., & Yorke, H. W. 2007, *ARA&A*, **45**, 481